University of Alberta

Development of a Clinical MRI Dosimeter

by

Lara Michéle Dyke

A thesis submitted to the Faculty of Graduate Studies and Research in partial fulfillment of the requirements for the degree of Master of Science

in

Medical Physics

Department of Physics

Edmonton, Alberta

Fall 1997

National Library of Canada
Acquisitions and Bibliographic Services
395 Wellington Street
Ottawa ON K1A 0N4
Canada

Bibliothèque nationale du Canada
Acquisitions et services bibliographiques
395, rue Wellington
Ottawa ON K1A 0N4
Canada

Your file Votre référence

Our file Notre référence

The author has granted a non-exclusive licence allowing the National Library of Canada to reproduce, loan, distribute or sell copies of this thesis in microform, paper or electronic formats.

L'auteur a accordé une licence non exclusive permettant à la Bibliothèque nationale du Canada de reproduire, prêter, distribuer ou vendre des copies de cette thèse sous la forme de microfiche/film, de reproduction sur papier ou sur format électronique.

The author retains ownership of the copyright in this thesis. Neither the thesis nor substantial extracts from it may be printed or otherwise reproduced without the author's permission.

L'auteur conserve la propriété du droit d'auteur qui protège cette thèse. Ni la thèse ni des extraits substantiels de celle-ci ne doivent être imprimés ou autrement reproduits sans son autorisation.

0-612-22592-5

Canada

University of Alberta

Library Release Form

Name of Author: Lara Michéle Dyke

Title of Thesis: Development of a Clinical MRI Dosimeter

Degree: Master of Science

Year this Degree Granted: 1997

Permission is hereby granted to the University of Alberta Library to reproduce single copies of this thesis and to lend or sell such copies for private, scholarly, or scientific purposes only.

The author reserves all other publication and other rights in association with the copyright in the thesis, and except as hereinbefore provided neither the thesis nor any substantial portion thereof may be printed or otherwise reproduced in any material form whatever without the author's prior written permission.

Lara Dyke

P.O. Box 284,
Kingston 8,
Kingston, Jamaica W.I.

July 11, 1997

University of Alberta

Faculty of Graduate Studies and Research

The undersigned certify that they have read, and recommended to the Faculty of Graduate Studies and Research for acceptance, a thesis entitled **Development of a Clinical MRI Dosimeter** submitted by **Lara Michéle Dyke** in partial fulfillment of the requirements for the degree of **Master of Science** in **Medical Physics**.

Dr. W. Ansbacher

Dr. G. Hughes

Dr. R. Sloboda

Dr. S. Halls

June 9, 1997 Date

to

my parents

Abstract

This thesis focuses on the development of an MRI gel dosimeter as a viable clinical dosimetry tool by establishing a usage protocol that will be easy to implement. This involved observing its clinical performance and performing a number of reference tests, taking into consideration phantom temperature conditions. Using $\Delta R2$, the difference between the spin-spin relaxation rate (R2) images of after and before irradiation, as a measure of dose, a $\Delta R2$ to dose conversion relationship was determined from measured data in the range of 5 Gy - 40 Gy, for orthovoltage and megavoltage photons, electrons, and a high dose rate Ir-92 source. The dose images can be used to construct depth doses and isodose distributions. The results indicate that this dosimeter can handle clinical irradiation set-ups effectively. In addition to observing its clinical performance, the dependence of the sensitivity of the dosimeter on the imaging frequency was investigated by measuring the relaxation rate for various concentrations of ferric and ferrous ions at imaging frequencies of 64 and 128 MHz.

Acknowledgments

First, I would like to thank my supervisors, Dr. Will Ansbacher, and Dr. G. Hughes, for their supervision during the past two years.

I would like to thank the members of the Medical Physics Department at the Cross Cancer Institute for their support and encouragement. I appreciated the help that Claire McCartney and Ernie Mah provided when problems arose with the computers or the computer programs, especially with Corel Draw (EM), as well as including me in those well needed coffee breaks. The technicians in the Machine Shop at the Cross Cancer Institute have my gratitude for their technical support. Also, the MRI technologists at the Cross Cancer Institute, Irene Piva and Doris Jeske, deserve my thanks for their time and patience in teaching me to operate the MRI scanner.

I would like to thank Mark Does and Caroline Tam of the Biomedical Engineering Department at the University of Alberta, for their time and expertise in acquiring the data at 3T.

The members of the examining committee have my gratitude for their many useful comments.

My best friend Philip deserves my appreciation and gratitude for his support and understanding when I had to work late, and for his proof-reading skills.

My sister Lisa deserves my thanks for her support and for picking me up after late nights at work.

Finally I would like to thank my labmates and colleagues, Parminder Basran, Isabelle Gagné, HJ Kim, John Kollar, Marc MacKenzie, and Collie Miller for their advice and support.

☺

Table of Contents

Introduction 1

1.1 Introduction to the Thesis *1*

1.2 Brief overview of Radiation Treatment Planning *2*

1.3 Motivation for a Volumetric Dosimeter *4*

Deposition and Measurement of Dose 9

2.1 Definitions of Kerma and Dose *10*

2.2 Charged Particle Equilibrium *12*

2.3 Deposition of Dose *12*

2.3.1 Interactions of Indirectly Ionizing Radiation with Matter 12

2.3.1.1 The Compton Effect 13

2.3.1.2 The Photoelectric Effect 14

2.3.1.3 Pair Production 15

2.3.2 Interactions of Directly Ionizing Radiation with Matter 15

2.4 Measurement of Dose *17*

2.4.1 Treatment Planning Beam Descriptors 17

2.4.1.1 Percent Depth Dose and the Tissue Phantom Ratio 18

2.4.1.2 Relative Dose Factor 19

2.4.1.3 Off-Axis Ratios and Beam Profiles 19

2.4.1.4 The Output Factor and the Stand-Off Factor 19

2.4.1.5 Calculation of Dose 20

2.4.2 Traditional Dosimetry Techniques 21

2.4.2.1 Ionization Chamber 21

2.4.2.2 Thermoluminescent Dosimeters 22

2.4.2.3 Film 23

2.4.2.4 Diodes 24

MRI Fricke Gel Dosimeter **31**

3.1 Development of the MRI Fricke Gel Dosimeter *32*

3.2 Radiation Chemistry of the Fricke Dosimeter *35*

3.3 NMR Theory of the Fricke Gel Dosimeter *37*

3.3.1 Spin-Spin Relaxation 39

3.3.2 Relaxation Effects due to Paramagnetic Ions 43

3.4 NMR Dosimetry of the Fricke Dosimeter *44*

3.5 Magnetic Resonance Imaging *45*

3.5.1 The Spin-Echo Sequence 45

3.5.2 Standard Imaging Protocol 47

Materials and Methods 53

4.1 Sample Preparation 53

4.2 Irradiation 54

4.3 Imaging and Measurement of Dose Distributions 55

4.3.1 Phantom Positioning and Temperature Considerations 56

4.3.2 Obtaining ΔR2 Images 57

4.3.2.1 Displaying ΔR2 Images 59

Clinical Performance 64

5.1 Investigation of the Dose Response due to Photon Beams 64

5.1.1 Uniformity of Dose Distributions 64

5.1.2 Dependence on Energy and Shape of Container 66

5.1.3 Linearity of Dose Response 66

5.1.4 Reproducibility and Accuracy 67

5.1.5 Diffusion effects 69

5.2 Investigation of the Dose Response for Electron Beams 70

5.3 Investigations of the Dose Response for an Ir-192 Brachytherapy Source 72

5.4 Clinical Applications 73

5.4.1 Head and Neck Study 73

5.4.1 Two Catheter Brachytherapy Study 74

Investigation of Relaxivity of Ferric and Ferrous Ions 91

6.1 Materials and Methods *91*

6.2 Results and Discussion *92*

Summary and Conclusions 97

References 100

Appendix 106

List of Figures

		Page
Figure 1.1	A typical percent depth dose curve	7
Figure 1.2	A typical isodose distribution	8
Figure 2.1	Charged particle equilibrium	25
Figure 2.2	Relative importance of the three main interactions of indirect ionizing radiation with matter	26
Figure 2.3	Compton effect	27
Figure 2.4	Photoelectric effect	28
Figure 2.5	Pair production	29
Figure 2.5	Tissue Phantom Ratios and Percent Depth Doses	30
Figure 3.1	Effects of a rf pulse	49
Figure 3.2	Transition probabilities between eigenstates	50
Figure 3.3	A spin-echo pulse sequence	51
Figure 3.4	Imaging pulse sequence	52
Figure 4.1	Set-up for photon irradiations	60
Figure 4.2	Imaging plane of the Fricke gel phantom	61
Figure 4.3	Orientation of phantom in the MRI scanner	62
Figure 4.4	An isodose distribution measured by the MRI gel dosimeter	63
Figure 5.1	Variation of dose along the axis of the beam	77

Figure 5.2	Absorbed dose versus ΔR2	78
Figure 5.3	Short and long term reproducibility	79
Figure 5.4	Depth dose curve for 200 kV photons	80
Figure 5.5	ΔR2 profile	81
Figure 5.6	Dose profiles at various post-irradiation imaging times	82
Figure 5.7	Measured beam penumbra widths as a function of time	83
Figure 5.8	Depth dose curves for a 9 MeV electron beam	84
Figure 5.9	Depth dose curves for 9, 12, and 18 MeV electron beams	85
Figure 5.10	Dose profile along the perpendicular bisector of a brachytherapy source	86
Figure 5.11	Irradiation set-up for a head and neck study	87
Figure 5.12	Dose profile generated by delivery of an electron and photon beam in a head and neck study	88
Figure 5.13	Isodose distribution in a head and neck study	89
Figure 5.14	Dose distribution for a two catheter brachytherapy irradiation	90
Figure 6.1	R2 vs. Fe3+ at 1.5 T and 3 T	94
Figure 6.2	R2 vs. Fe2+ at 1.5 T and 3 T	95
Figure 6.3	Relaxivity of ferric and ferrous ions versus proton resonance frequency	96

List of Tables

		Page
Table 5.1	a) ΔR2 data for phantoms irradiated to dose levels of 5 to 15 Gy b) ΔR2 data for phantoms irradiated to dose levels of 20 to 40 Gy	76

List of Abbreviations

CCI	Cross Cancer Institute
CPMG	Carr-Purcell-Meiboom-Gill
CT	Computed Tomography
FOV	Field of View
HDR	High Dose Rate
ICRU	International Commission on Radiation Units and Measurements
Kerma	Kinetic energy released in matter or a medium
LDR	Low Dose Rate
Linac	Linear Accelerator
MRI	Magnetic Resonance Imaging
MU	Monitor Unit
NMR	Nuclear Magnetic Resonance
OAR	Off-axis Ratio
OD	Optical Density
OF	Output Factor
PDD	Percent Depth Dose
RDF	Relative Dose Factor
SOF	Stand Off Factor
SSD	Source to Surface Distance
TLD	Thermoluminescent Dosimeter
TPR	Tissue Phantom Ratio

List of Symbols

$\Re 2$	Relaxivity for spin-spin interaction
B_0	Main magnetic field
B_1	The alternating magnetic field or rf field
D	Absorbed Dose
δ	Delta ray
$\delta R2$	Change in spin-spin relaxation rate due to differences in ion relaxivities
$\Delta R2$	Difference in spin-spin relaxation rate before and after irradiation
γ	gyromagnetic ratio
h	Planck's constant
I	spin angular momentum
K	Kerma
κ	Pair production interaction cross-section
μ	linear attenuation coefficient
μ	magnetic moment
ν	frequency
ρ	density
R1	Spin-lattice relaxation rate
R2	Spin-spin relaxation rate
σ	Compton effect interaction cross-section
τ	Photoelectric effect interaction cross-section
T1	Spin-lattice relaxation time
T2	Spin-spin relaxation time
ω_0	Larmor frequency
Ψ	Energy Fluence
Z	Atomic number

Chapter 1

Introduction

1.1 Introduction to the Thesis

Radiation therapy is one of the main methods used in the treatment of cancer. It involves using ionizing radiation to kill tumour cells. The two modes of delivery of the radiation are teletherapy and brachytherapy. Teletherapy is the delivery of radiation from a large distance, using a machine located external to the patient, usually a Linear Accelerator (Linac). The most common radiation fields used for teletherapy are photons and electrons. Brachytherapy is the delivery of radiation from a short distance, i.e. immediately adjacent to or within the patient. A brachytherapy source, moulded intc an applicator, is a radioactive isotope that emits γ–rays.

In order to assess the efficacy of the radiation dose, the distribution of energy deposited in the body should be determined to ensure that the tumour receives the maximum possible dose, while a minimal dose is delivered to the surrounding healthy tissue. A number of techniques have been developed to measure this energy deposition. With many techniques, a substitute for the human body is used, which is known as a phantom. An important criterion for a phantom is that it should be composed of material that will absorb and scatter photons in the same way as tissue [Johns and Cunningham 1983]. The most common phantom used is water because it behaves in almost exactly the same way as soft tissue, which is composed of 75 - 90% water [Tortora 1992]. With water phantoms, an external probe or dosimeter is needed to actually measure the absorbed energy. The most common dosimeter that is used

for absolute dosimetry is the ion chamber, which will be described in more detail in Section 2.4.2.

In this work, a combination of a chemical dosimeter and phantom will be investigated for the purpose of evaluating its viability in the clinical environment. The combined dosimeter and phantom is known as the Magnetic Resonance Imaging (MRI) Fricke gel dosimeter. The gel matrix acts as the phantom while the infused Fricke solution, a ferrous sulphate solution, acts as the dosimeter. The phantom is tissue/water equivalent [Chan and Ayyangar 1993] and can be used to model what will occur in human soft tissue. Fricke solution is widely used as an absolute dosimeter and its dose response is well known. Upon irradiation, the ferrous ions present in solution oxidize to ferric ions. This chemical reaction will be discussed in Section 3.2. A clinical MRI scanner is utilized to measure the dose response and display the spatial distributions of the dose. The parameter that is used as a measure of dose is the spin-spin relaxation rate, R2 of protons in the water molecules. The theory of MRI relevant to this work will be discussed in Section 3.3. The dosimeter was investigated by observing its ability to reproduce the same dose distributions over a period of time, as well as its ability to accurately determine the dose at a point. Also, investigations were conducted to ensure that there was no dependence on the energy of the beam or the type of container used for irradiation, and that the dosimeter could handle clinical cases. Investigations were conducted to provide guidelines for imaging times and phantom temperature conditions.

The subsequent sections of this chapter provide an overview of treatment planning and the motivation for the development of this dosimeter

1.2 Brief overview of Radiation Treatment Planning

In order to successfully treat cancer using radiation, the best method of delivery must be determined. This includes determining the most appropriate type of

radiation, the correct dosage and the size and shape of the radiation field. Treatment planning is the process by which all of this is accomplished.

An important part of treatment planning is the correct placement of beams. The beam or radiation field can be characterized by its dose distribution. When one or more beams are placed in combination, their dose distributions add to produce a combined dose distribution. In order for the process to be as successful as possible, dose distributions must be known accurately. Depth dose curves illustrate the variation of absorbed dose with depth within a patient or phantom, two examples of which are shown in Figure 1.1. Central axis depth doses are characterized by normalizing the dose to 100% at a reference depth, which is usually taken to be d_{max}, the depth at which the dose is at its maximum. In a two-dimensional representation, isodose distributions are curves connecting points of equal dose. The curves are drawn at equal increments of percent depth dose, which represents the variation in dose as a function of depth and transverse distance from the central axis. An example of an isodose distribution is shown in Figure 1.2. Some of the factors that affect isodose distributions and depth doses are beam energy, source size, source to surface distance (SSD) and beam attenuation. A more detailed description of these beam descriptors will be provided in Section 2.4.1.

The standard conditions for obtaining depth doses and isodose distributions are the following: using a homogeneous unit density phantom and placing the beam perpendicular to the flat surface of the phantom at a fixed distance from the source. The information obtained from this irradiation set-up does not truly model what happens in the human body, but it is accurate to a first approximation when used as reference data [Khan 1994]. So, in addition to the information obtained from these distributions, patient information has to be factored in to ensure dose uniformity in the irradiated volume at treatment time. Patient contours and tissue electron densities are obtained through Computed Tomography (CT). Given information about tissue inhomogeneities and body contours, a number of correction algorithms are implemented to modify the reference dose distributions. The algorithms correct for

beam attenuation and scattering, and changes in SSD. These modified dose distributions are used in the treatment planning process.

1.3 Motivation for a Volumetric Dosimeter

Because treatment planning algorithms have some limitations, there is a need for a dosimeter that can obtain data under non-standard conditions. The dosimeter will be required to handle any beam energy, geometry and orientation. New advances in the field of radiotherapy have supplemented traditional beams with beams that are time-varying (dynamic) or shaped to the outline of the tumour (conformal). These beams require a dosimeter that can measure their characteristics effectively before they can be implemented in clinical practice. The dosimeter in question should be able to integrate the dose in a three-dimensional volume for maximum efficiency.

Traditional dosimeters used to measure dose distributions include ion chambers, diodes, thermoluminescent detectors (TLDs), and film. These dosimeters have limitations that prevent them from handling the latest beams easily and accurately. Ion chamber and diode arrays can provide good dose distributions in one dimension but require the array to be moved in the other two directions to obtain the whole field of view. The response of diodes is energy dependent, which is an additional problem. TLDs can be used although a large number would be required to cover a three-dimensional volume. Film, which is a two-dimensional dosimeter, requires that each new batch be calibrated. Also, film has a dose response that is energy dependent; this is seen as an over-response in the low energy region.

Integrating dosimeters are those that are able to measure the dose at a certain point over a period of time while the radiation is being delivered. All the above dosimeters can do this. Real time dosimeters, ion chambers and diodes, are also able to provide information about dose as it is being delivered when the dose is sampled over the period of time.

Point dosimeters are those that will measure a dose at a certain point in space. Examples of point dosimeters are ion chambers, diodes and TLDs. One-dimensional dosimeters are those that are able to measure dose along a certain line in space. This is usually accomplished by the use of either an ion chamber or diode array. One way to obtain planar distributions is to use one-dimensional dosimeters and move them along the axis perpendicular to the array. Another way is to use film, which provides good two-dimensional distributions without the added nuisance of moving it in space. Volumetric dosimeters are dosimeters that are able to measure dose at every point in a volume, but doing so is difficult and time consuming when using arrays or film. With film, one would not be able to obtain a full volumetric distribution because of the need to sandwich the film between the phantom materials. The proposed dosimeter in this thesis, the MRI gel dosimeter, would be able to obtain volumetric dose distributions because MRI has the capabilities of obtaining a number of two-dimensional slices or three-dimensional volumes. Although the possibility exists to read out the dosimeter in three dimensions, this dosimeter is presently being read to provide multiple two-dimensional distributions.

To determine whether the MRI gel dosimeter could be implemented in the clinical setting, several important questions need to be answered, including:

- can the dose response of the system be accurately reproduced and how does it depend on beam energy and gel container size?
- is the dose response the same for electrons as for photons?
- what effect does oxygenation and ion diffusion have on the measured dose distributions?
- what protocol must be used to obtain accurate information on dose distributions in clinical cases? What is the accuracy of the measurement? The reproducibility?
- how does the sensitivity of the dosimeter depend on the imaging frequency?

In response to these questions, changes in R2 caused by irradiation were used to determine the dosimeter's capabilities. A description of the protocol for obtaining dose distributions is discussed in Chapter 4. The results of investigations of the dosimeter's capabilities and characteristics will be presented and discussed in Chapter 5. Chapter 6 provides a discussion of the dependence of the sensitivity of the dosimeter on imaging frequency. A summary and some conclusions are presented in Chapter 7.

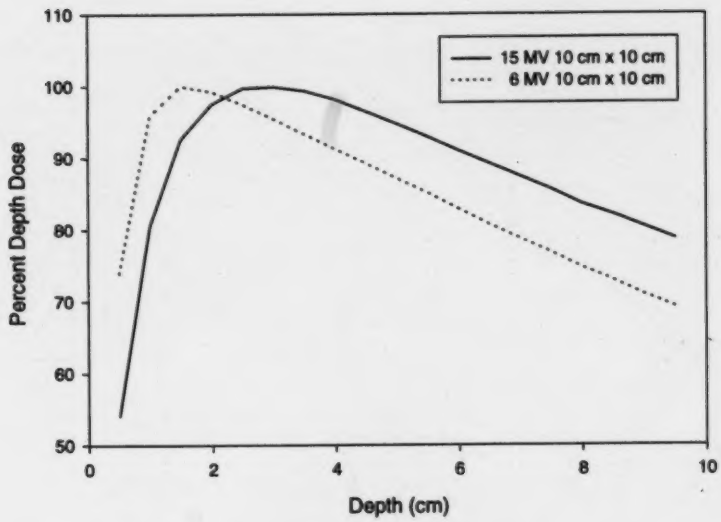

Figure 1.1: Central axis Percent Depth Dose (PDD) curves for typical 10 cm x 10 cm photon beams of energy 6 MV and 15 MV.

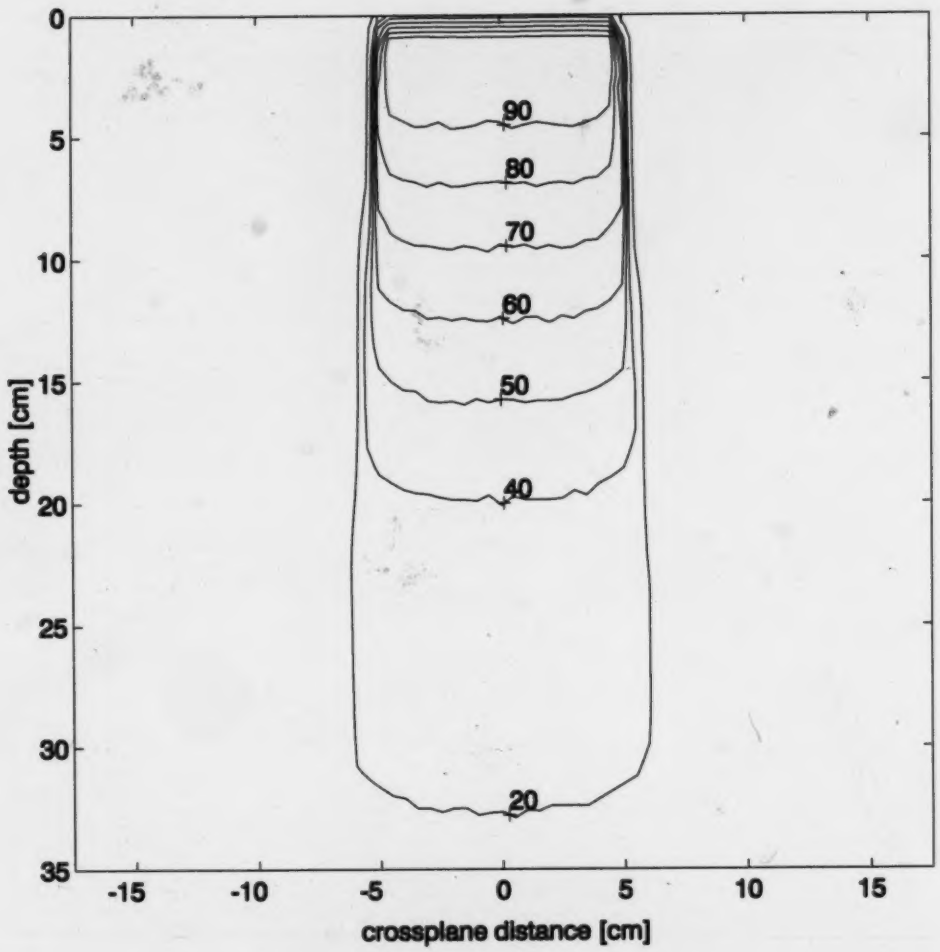

Figure 1.2: An isodose distribution for a typical 10 cm x 10 cm 6 MV photon beam. The distribution is normalized to 100% at a depth of 1.5 cm on the central beam axis.

Chapter 2

Deposition and Measurement of Dose

Since the topic of this thesis is the MRI gel dosimeter, a discussion on the mechanism of energy deposition is warranted. This chapter will focus on the interactions of radiation with matter, which are the means by which energy is deposited. It will also contain an overview of treatment planning beam descriptors and an in-depth description of traditional dosimeters.

In radiotherapy dose may be deposited by electrons, γ-rays, x-rays, protons, neutrons, and a number of other heavy charged particles. These particles and photons are classed as ionizing radiation, which is any radiation that has the ability to excite or ionize atoms of the matter through which it passes. The minimum energy required to eject an electron from an atom is approximately 4 eV. Therefore, any particles that possess kinetic energy greater than 4 eV are considered to be "ionizing radiation". Similarly, photons whose photon energy, hν, is greater than 4 eV can be considered to be "ionizing radiation".

The group can be further sub-divided into two groups: directly and indirectly ionizing radiation. Charged particles are considered to be directly ionizing radiation since they have the ability to disrupt the atomic structure through which they travel and produce chemical and biological changes. Conversely, x-rays and γ-rays are classified as indirectly ionizing radiation because they do not directly cause biological and chemical damage, but interact with charged particles that will in turn produce damage.

2.1 Definitions of Kerma and Dose

Before discussing the interactions of radiation at the atomic level, there are two quantities that need to be defined. These quantities describe the interactions of the radiation field with matter. They are kerma, K, which stands for kinetic energy released in a medium (the a is there for phonetic reasons) [Johns and Cunningham 1983] and absorbed dose, D. Kerma and absorbed dose are measured in units of J/kg, which is known as a Gray (Gy).

Kerma is the amount of energy transferred from indirectly ionizing radiation to charged particles per unit mass of tissue or matter. It is usually written in the following form:

$$K = \frac{dE_{tr}}{dm}. \tag{2.1}$$

Radiation fields can be described in terms of energy fluence, Ψ, which is the total amount of energy per unit area of beam and whose units are Jm^{-2}. This energy fluence, Ψ, will undergo simple exponential attenuation when it travels through medium of thickness L and whose associated attenuation coefficient is μ [Attix 1986]. Kerma can therefore be written in terms of energy fluence, and its effects:

$$K = \Psi\left(\frac{\mu_{tr}}{\rho}\right)_{E,Z}, \tag{2.2}$$

where (μ_{tr}/ρ) is the mass energy transfer coefficient which is characteristic of both the photon energy, E, and the matter, whose atomic number is Z, with which it interacts. The units of the mass energy transfer coefficient are m^2/kg. Kerma can be further divided into terms that describe whether the energy has been dissipated nearby, K_c, or has been carried away by radiation, K_r. Radiative Kerma, K_r, is therefore the

difference between kerma and collision kerma. Collision kerma, K_c, describes the net energy transferred to charged particles at the point of interest. It does not include any radiative-loss energy or energy passed from one charged particle to another. Collision kerma can also be expressed in terms of Ψ:

$$K_c = \Psi\left(\frac{\mu_{en}}{\rho}\right)_{E,Z}, \tag{2.3}$$

where (μ_{en}/ρ) is the mass-energy absorption coefficient. The mass-energy transfer and absorption coefficients are the sum of the three dominant interactions: pair production, Compton scattering and photoelectric effect. For low energies (μ_{en}/ρ) is equal to (μ_{tr}/ρ), but as the energy of the incident beam increases these terms deviate from each other because of energy that is lost due to radiative interactions. The two coefficients can be related by:

$$\frac{\mu_{en}}{\rho} = \frac{\mu_{tr}}{\rho}(1-g), \tag{2.4}$$

where g is the fraction of energy lost due to radiative interactions.

Absorbed dose, D, describes the amount of energy that is actually retained in the medium, and therefore is different from kerma. It is written as:

$$D = \frac{dE_{ab}}{dm}. \tag{2.5}$$

The absorbed dose is relevant to all types of radiation fields, either directly or indirectly ionizing radiation, and any radiation source distributed within the absorbing medium. Unfortunately, it cannot in general be expressed in terms of fluence or energy fluence as was done for kerma and collision kerma. However, when charged

particle equilibrium occurs (see section 2.2), the absorbed dose is equal to the collision kerma, or

$$D \cong K_c . \tag{2.6}$$

2.2 Charged Particle Equilibrium

Charged particle equilibrium, also known as electronic equilibrium, is the condition under which absorbed dose is equal to collision kerma. The requirement for charged particle equilibrium is that the number of charged particles of a given type and energy entering a volume of interest is equal to the number of charged particles of that type and energy leaving the volume as shown in Figure 2.1. The significance of charged particle equilibrium is that, if it exists, the absorbed dose can be calculated when the photon fluence and energy are known. If charged particle equilibrium does not exist, the absorbed dose cannot be calculated from the photon fluence and energy.

2.3 Deposition of Dose

Dose is deposited through the interactions of ionizing radiation with matter. Therefore, a brief discussion will be provided on the mechanisms of interaction for both indirectly and directly ionizing radiation with matter.

2.3.1 Interactions of Indirectly Ionizing Radiation with Matter

In radiological physics there are three main types of interactions of γ- and x-ray photons with matter that have to be considered. These are the Compton effect, photoelectric effect, and pair production. These three interactions result in the

transfer of energy to electrons. The cross section of any interaction is a measure of the probability of that interaction occurring. Each of these interactions, by way of its cross section, contributes to the coefficients of mass attenuation (μ/ρ), mass-energy transfer (μ_{tr}/ρ), and mass-energy absorption (μ_{en}/ρ). These interactions will be discussed below in more detail.

The probability of each of these interactions occurring is dependent on the energy of the beam and Z_{eff}, the electron-fraction-weighted-average atomic number of the atoms in the absorbing material [Attix 1986]. The Z_{eff} of water is 7.51 [Johns and Cunningham 1983] whereas the Z of the MRI dosimeter is approximately 7.48 [Duzenli 1995]. For such low values of Z and for photons in the range 20 keV to 30 MeV, the Compton effect is dominant, as shown in Figure 2.2.

2.3.1.1 The Compton Effect

The Compton effect describes the interaction in which an incident photon gives up part of its energy to a weakly bound electron which is ejected from the atom. The incident photon is scattered, as shown in Figure 2.3, with energy that is equal to that of the original quantum less the recoil energy of the electron. The probability of a Compton interaction occurring is governed by the Klein-Nishina (K-N) cross section, which is heavily dependent on the energy of the incident photon beam (hv) and photon scattering angle θ. The Compton mass attenuation coefficient, σ/ρ, is given by:

$$\frac{\sigma}{\rho} = \frac{N_A Z}{A} \cdot \sigma, \tag{2.7}$$

where N_A is Avogadro's number, A is the average mass number of the nuclei in the material, Z is the average atomic number, and ${}_e\sigma$ is the total K-N cross section per electron.

The energy transfer coefficient, (σ_{tr}/ρ), describes the amount of energy that is transferred to the recoil electron. This term is determined from a modification of the differential K-N cross section and yields $({}_e\sigma_{tr}/\rho)$, the K-N energy-transfer coefficient. The Compton mass energy transfer coefficient can now be written as:

$$\frac{\sigma_{tr}}{\rho} = \frac{N_A Z}{A} \cdot {}_e\sigma_{tr} . \tag{2.8}$$

2.3.1.2 The Photoelectric Effect

The photoelectric effect describes the interaction that occurs when an incident photon relinquishes all of its energy to an atomic electron. The electron is usually in the K-shell and is subsequently ejected, as shown in Figure 2.4. The energy of the electron is that of the incident photon minus the binding energy of the electron.

The cross section for the photoelectric effect is not easily derived and most tables consist of values obtained from experimental data. In the energy region in which the photoelectric effect is dominant, that is for energies less than about 0.1 MeV, the photoelectric mass attenuation coefficient, τ/ρ, is found to be proportional to $(Z/h\nu)^3$, i.e.:

$$\frac{\tau}{\rho} \propto \left(\frac{Z}{h\nu}\right)^3 , \tag{2.9}$$

where $h\nu$ is the energy of the incident photon.

2.3.1.3 Pair Production

For photons whose energy is greater than 1.02 MeV, there is a probability that the photon will be completely absorbed through the mechanism of pair production. Pair production occurs when a photon passes near the nucleus of an atom and is subject to strong nuclear fields. The photon may suddenly disappear and emerge as a positron-electron pair, as shown in Figure 2.5. Charge is conserved because the lepton pair has opposite charges. Any energy in excess of 1.02 MeV is shared between the pair. Energy and momentum cannot be conserved simultaneously. Therefore, when discussing the production of a positron-electron pair, only energy is conserved and when one includes the nucleus into the system, only momentum is conserved. The probability of pair production occurring, measured by the pair production coefficient, κ, is proportional to Z^2 per atom or to Z per electron or per gram.

2.3.2 Interactions of Directly Ionizing Radiation with Matter

Unlike indirectly ionizing radiation, the chance of interactions of charged particles occurring with matter is considerably greater due to the Coulomb-force field that surrounds the particles. A charged particle will interact with the electrons and nuclei of atoms in the immediate vicinity of its path. With each of these interactions, only a fraction of the charged particle's initial kinetic energy is relinquished, and the particle therefore interacts with many atoms before coming to rest. The term *pathlength* describes the length of the path which these particles take through matter. Another term, *range*, describes the expected distance that these particles will travel before eventually coming to rest. Because of the nature of these particles, their paths are not usually straight, and not even identical particles will follow the same path.

For electrons, especially, since their mass is quite small, there is a considerable amount of scattering within the medium.

The interactions of charged particles with matter can be divided into three main categories: soft collisions, hard collisions, and coulomb-force interactions with the external nuclear field. These three interactions are incorporated into the expression for the mass stopping power, used to describe the rate at which energy is lost per unit length: $(dT/\rho dx)_{Y,T,Z}$, Y, T, Z signifying that it is heavily dependent on the type of particle, Y, the particle's kinetic energy, T, and the Z of the material. The mass stopping power is usually measured in MeV $cm^2 g^{-1}$. The mass stopping power is usually further divided into the mass collision stopping power, subscript c, and the mass radiative stopping power, subscript r:

$$\left(\frac{dT}{\rho dx}\right)=\left(\frac{dT}{\rho dx}\right)_c+\left(\frac{dT}{\rho dx}\right)_r. \tag{2.11}$$

The mass radiative stopping power describes the rate at which bremsstrahlung is produced by electrons and positrons. Bremsstrahlung, also known as braking radiation, are x-rays produced as the electron or positron decelerates [Attix 1986]. Only electrons and positrons produce bremsstrahlung due to their small mass. The mass radiative stopping power term is essentially zero for other charged particles.

So-called soft collisions occur when the closest distance of approach, or the impact parameter, is several atomic radii or greater. In this interaction the Coulomb force field of the charged particle affects the atom as a whole. The consequence is that the atom is either excited to a higher energy level or becomes ionized through the ejection of a valence electron. Only a small fraction of the charged particle's energy is transferred to the absorbing matter in a single interaction. But because large numbers of such interactions occur, they account for more than half of the energy transferred to the absorbing matter.

Hard collisions, also known as "knock-on" collisions, occur with the electrons in an atom when the impact parameter of the particles is on the order of the atomic radius. These electrons are ejected from their orbits with a considerable amount of energy. These ejected electrons are called delta rays (δ-rays). Also, characteristic x-rays and/or Auger electrons can be produced if the ejected electron originates from an inner shell. The fraction of energy dissipated via this interaction is comparable to that of the soft collision interactions, even though its probability is much less than that of soft collisions.

When a charged particle approaches the nucleus of an atom, the particle is scattered either elastically, resulting in no energy loss, or inelastically, resulting in the ejection of an x-ray photon. This interaction occurs most frequently with electrons. Due to the high percentage of the interactions that result in elastic scattering, the electrons follow very tortuous paths. This tendency increases with large Z and causes substantial backscattering. When the interaction results in inelastic scattering, which occurs a very small percentage of the time, a significant amount of energy is given up which results in the production of bremsstrahlung.

2.4 Measurement of Dose

2.4.1 Treatment Planning Beam Descriptors

In treatment planning, a number of methods are used to calculate dose in a patient. For photon beams, these methods include percent depth dose and tissue-phantom ratio. Percent depth dose was the first method used to calculate dose, but due to limitations that included dependence on SSD, the tissue-phantom ratio (TPR) evolved. The machines used in the delivery of radiation, Linacs, are isocentric which means that the distance from the source to the treatment location is fixed. This feature of the Linacs also warranted a better beam descriptor such as TPR. This

section will focus on describing these two methods used in photon beam calculations, as well as describing the relative dose factor, another term used in these calculations. The parameters used in electron beam dose calculations will also be discussed.

2.4.1.1 Percent Depth Dose and the Tissue Phantom Ratio

In the field of treatment planning, one way to characterize the dose along the central axis of the beam is to normalise the dose at a given depth with respect to a reference depth. This ratio, expressed as a percentage, is known as the percent depth dose, PDD, and is written in the form

$$PDD = \frac{D_d}{D_{d_0}} \times 100\%, \tag{2.12}$$

where D_d is the dose at depth d and D_{do} is the dose at the reference depth d_0 [Khan 1994]. For megavoltage beam energies, d_0 is taken to be the depth of the peak absorbed dose, d_{max}. Also, PDDs are used in electron beam therapy and the same definitions hold.

There are a number of parameters that affect the PDD which include depth in the phantom, field size and shape, the source-surface distance (SSD), and beam energy. The dependence on the SSD is due to the fact that the photon fluence emitted by a point source of radiation varies as the inverse square of the distance from the source. Therefore when using different SSDs, a correction factor, known as the Mayneord F Factor, must be applied to convert the PDD obtained from standard conditions to that needed in the treatment conditions [Khan 1994].

The tissue-phantom ratio is defined as "the ratio of the dose at a given depth in the phantom to the dose at the same point at a fixed reference depth, usually 5 cm or d_{max}" [Khan 1994]. This concept is illustrated in Figure 2.6. Using the TPR

eliminates the dependence on SSD because the measurement point is fixed and the beam divergence, which is due to SSD, does not have much of an effect. TPR is only used in the photon dose calculations because it is not relevant for electrons.

2.4.1.2 Relative Dose Factor

The relative dose factor, RDF, includes the factors, excluding those that encompass patient contour and inhomogeneity information, that are needed to relate the change in dose between the standard calibration conditions to the treatment conditions at the reference depth. This factor accounts for changes in the output of the machine due to field size effects.

2.4.1.3 Off-Axis Ratios and Beam Profiles

Previously the discussion was focused on beam descriptors that dealt with defining the dose along the axis of the beam. However there is a variation of the dose across the field which is usually depicted as a beam profile. The term that is used to determine the dose at a point that does not lie along the beam axis is known as the *off-axis ratio* (OAR). Off-axis ratios are derived from cross-beam profiles measured at a number of depths in a phantom for the largest field size available. Therefore OARs are defined as the ratio of dose at the off-axis point of interest to the dose at the central axis at the same depth [Khan 1994].

2.4.1.4 The Output Factor and the Stand-Off Factor

The following section will discuss the beam descriptors that are relevant only to electron dose calculations. The output factor (OF) and the stand-off factor (SOF) are used in the calculation of dose delivered to a specified point in the patient, which

is usually d_{max}. The output factor relates the change in dose between the standard or calibration field to the treatment field. It gets dramatically smaller as the field size of the beam decreases but is nearly constant for large field sizes, because of electrons scattering out of the field [Khan 1994].

For electron beam therapy, there is no well defined source so an "effective" source distance is used and the output factor is related to this distance. Therefore instead of using the inverse square law to determine the dose delivered when the SSD is not equal to 100 cm, a measured stand-off factor is used.

2.4.1.5 Calculation of Dose

Now that a discussion has been provided of the different beam descriptors, a description of how dose is calculated is warranted. In treatment planning, a term known as a monitor unit (MU) is used to calculated the dose delivered.

The output of a Linear accelerator (Linac) is not stable and therefore the beam must be continually monitored. This is accomplished by placing monitor chambers, which are essentially ionization chambers, close to the x-ray target or electron scattering foil in the head of the Linac so that the entire beam passes through them. A monitor unit (MU) is a measure of the accumulated charge that results. Linacs at the CCI are calibrated to deliver 1 cGy/MU at d_{max} with a 10 cm x 10 cm field 100 cm away from the source under standard conditions. The number of monitor units that were delivered for the photon studies was calculated using the following relationship, which is a modification of the formula by Khan [1994]:

$$MU = \frac{\text{Dose}}{\text{RDF(fs)xTPR(d, fs)}}. \qquad (2.13)$$

RDF is the relative dose factor that is a function of field size (fs) and is equal to one for a 10 cm x 10 cm field. TPR is the Tissue Phantom Ratio, which gives the fraction of dose that is expected at a certain depth (d) and particular field size. For the electron studies, the monitor units were calculated using the following relationship [Khan 1994]:

$$MU = \frac{\text{Dose}}{(OF)\times(SOF)}, \tag{2.14}$$

where (OF) is the output factor for the particular electron applicator and (SOF) is the stand-off factor, which is an effective inverse square factor, if the SSD is not equal to 100 cm.

2.4.2 Traditional Dosimetry Techniques

Before the MRI Fricke gel dosimeter was developed in 1984 [Gore *et al.* 1984], other dosimeters were already being used to measure dose rate and dose distributions. Many of these other dosimeters are still used today as they are very good detectors, and are capable of handling most traditional beam geometries that are being used for treatment. These dosimeters include the ionization chamber, the diode, film, and thermoluminescent dosimeter (TLD), and they will be reviewed in this section. An overview of the various dosimetry techniques can also be found in the literature [Johns and Cunningham 1983, Attix *et al.* 1986, Stanton *et al.* 1992].

2.4.2.1 Ionization Chamber

The ionization chamber is a highly precise dosimeter that is widely used in the field of radiotherapy. The chamber consists of a gas, usually air, and two electrodes

which are responsible for collecting the ions created in the gas. The traditional ionization chamber is the thimble chamber, which has a central electrode surrounded by wall material. The molecules of the gas are ionized by an incoming radiation beam. Ion pairs arise from this ionization, the positive ions being collected on the negative electrode and the negative ions collected on the positive electrode. The amount of charge collected is proportional to the amount of radiation that is imparted. A voltage of about 300 V must be applied across the electrodes in order for the ion pairs to be collected, due to the tendency of the ion pairs to recombine when there is little or no voltage.

The efficiency of the dosimeter increases as the amount of recombination decreases. The charge produced per ion pair is proportional to the energy absorbed in the chamber over a wide range of photon/electron energies. The ratio of energy per unit charge, known as (W/e), is found experimentally to be 33.97 J/C in air. This allows for accurate measurement of dose. An added advantage of this dosimeter is that air is nearly tissue equivalent. This does not suggest that corrections for air cavities such as those found in the human body should be ignored because the size of the ionization chamber air cavity is small, 0.1 - 0.3 cm^3, and therefore is said not to disrupt the photon fluence in the medium. For use of these chambers at high energies, a build-up cap is placed over the chamber. Made out of material that is similar to air or tissue, this build-up cap aids in the establishment of electronic equilibrium. The thickness of the build-up cap depends on the energy of the incident beam. Ionization chambers are used as the "standard" against which most other dosimetry techniques are calibrated.

2.4.2.2 Thermoluminescent Dosimeters

Thermoluminescent dosimeters, TLDs, are mainly composed of lithium fluoride in two major forms: powder and shaped solids. At the atomic level, the

lithium fluoride atoms form a crystalline pattern which is called a lattice. The electrons are shared in this lattice pattern, and when exposed to irradiation the electrons move from their atomic location to locations called traps, where they remain until the dosimeter is heated. When the electrons are released through the heating process, they travel to the conduction band and then fall to their lattice ground states, emitting light. This light is measured by a photomultiplier tube in units of electric charge and is proportional to the amount of radiation that was absorbed, expressed in cGy. Fortunately, TLDs may be reused but at the cost of losing the information; consequently, they can only be read out once. Benefits of TLDs are that they are nearly independent of dose-rate and have a wide dynamic range. Also they are nearly tissue equivalent. For patient monitoring in Radiotherapy, the typical size of a TLD shaped into a chip is 3 mm x 3 mm x ½ mm[1]

2.4.2.3 Film

Film, also known as photographic emulsions, consists of microscopic grains of silver bromide dispersed in a gelatin layer on either or both sides of a supporting film. The reaction that takes place when a beam is incident on film is that Ag^+ ions are converted to Ag atoms. A latent image is produced and now the film is ready to be developed. During the developing process all remaining ions are reduced to silver atoms and the bromine is removed. The grains that have the latent image will have the ions reduced more rapidly. What is left is opaque silver that can be measured optically. Optical density (OD) is the parameter obtained from the transmission of light through the film and which is related to dose. Some advantages of film are that it has good spatial resolution, is dose-rate independent, and is easily obtained commercially. Some major disadvantages of film are that it has a strong dependence on the incident energy due the high Z of the material, the film batch and the processor.

---

[1] Lithium Fluoride TLD 100, Harshaw, U.S.A

The high Z of film increases the probability of photoelectric absorption occurring at low energies. Furthermore, air gaps can arise when placing film in a phantom and cause inaccuracies in measuring dose.

2.4.2.4 Diodes

Diodes, also known as semiconductor dosimeters, are solid state devices that measure dose and dose rate. The most common diodes used are silicon diodes with *p-i-n* junctions. The *p* region is where holes are located, the *i* region is called the intrinsic region, and the *n* region is where excess electrons are located. The diode is used either in a reversed-bias or an unbiased state. The incident radiation creates electron-hole pairs. The electrons are then elevated to the conduction band while the holes are left in the valence band. The resulting current which is related to the dose rate is measured by an electrometer. The signal that is produced when the radiation is applied is approximately 10 times greater than that produced in an ion chamber [Attix 1986]. This is due to the small amount of energy required to produce an ion pair (W/e) and the high density of the material. Unfortunately, like film, diodes have an energy dependence and therefore must be calibrated against an ion chamber. The advantages of diodes are that they have good spatial resolution and like TLD's can be placed on the skin of patients to measure localised surface doses. But unlike TLDs, diodes are able to read and display the dose immediately. These detectors can be used for both photons and electrons, but there is a different design for the two types of radiation fields. For electrons, the p-type diode, where the holes are the majority carrier and dominate the electrical conductivity, is used in dosimetry [Knoll 1989].

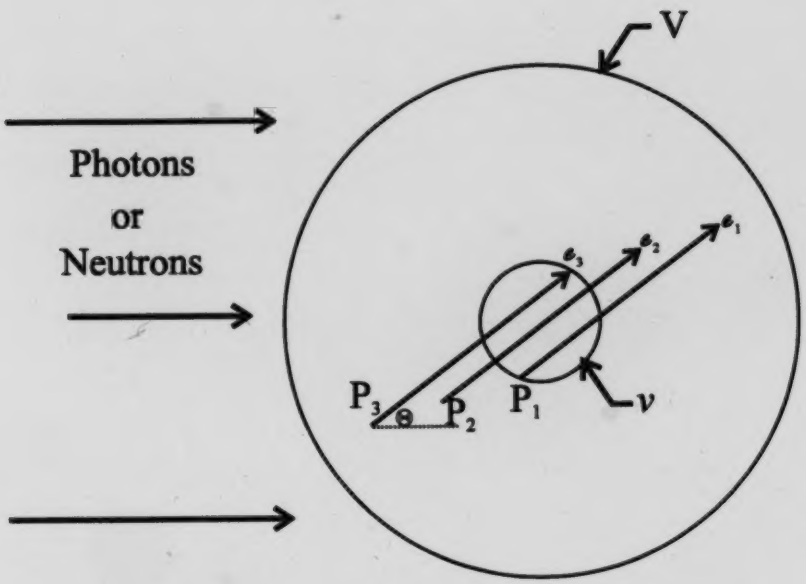

Figure 2.1: Charged particle equilibrium exists in v if the total energy dissipated in v by the three particles equals that which e_1 alone would have spent if its entire track had remained within v [Attix1986].

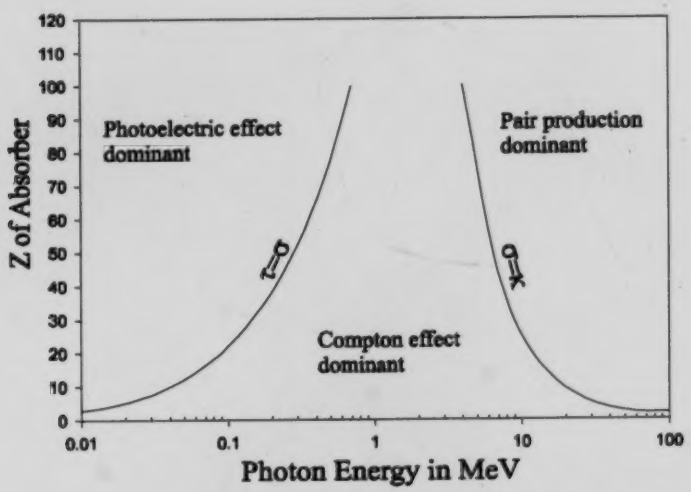

Figure: 2.2 A diagram representing the relative importance of the three main interactions in radiological physics, the Compton effect, photoelectric effect and pair production. The curve on the left hand-side indicates where the photoelectric mass attenuation coefficient, τ/ρ, equals the Compton mass attenuation coefficient, σ/ρ. Similarly, the right hand-side curve is where the Compton mass attenuation coefficient, σ/ρ, equals the pair production mass attenuation coefficient, κ/ρ. [adapted from Attix, 1986]

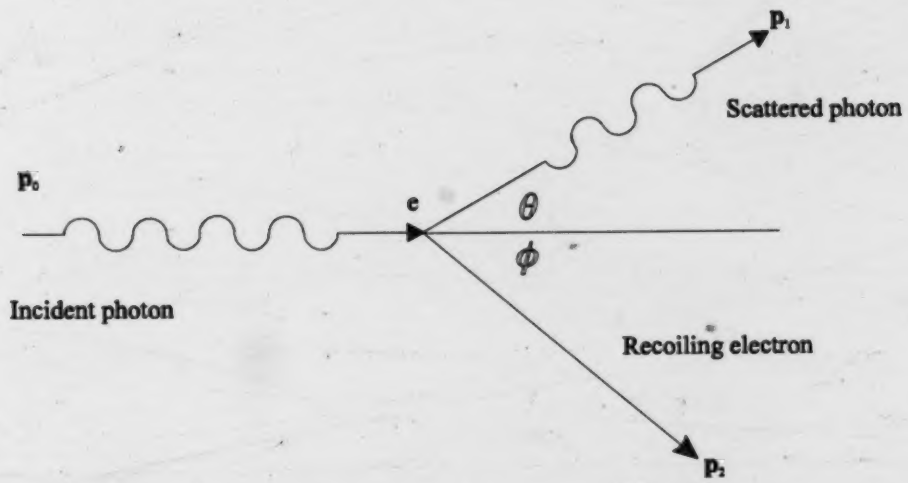

Figure: 2.3 A schematic diagram of the Compton effect. An incident photon with momentum, $\mathbf{p}_0$, strikes a stationary electron which then recoils with momentum $\mathbf{p}_2$. The scattered photon departs with momentum $\mathbf{p}_1$. [Attix, 1986]

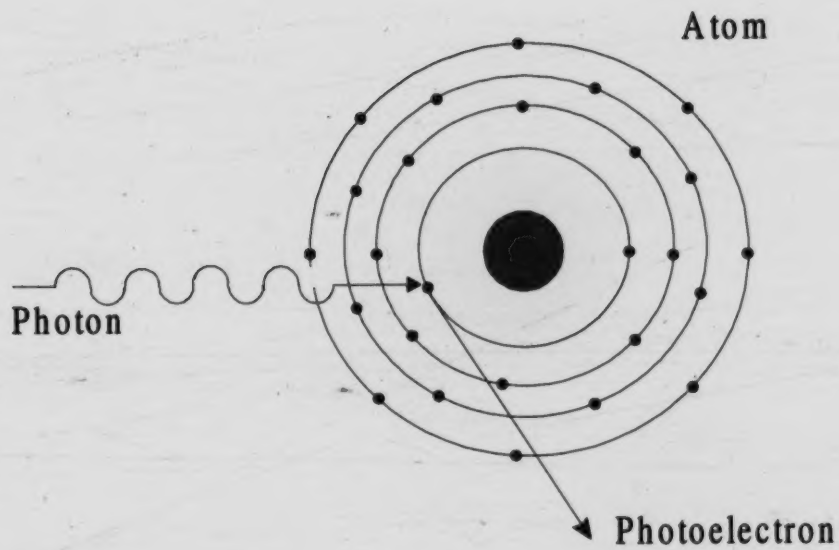

Figure: 2.4 The photoelectric effect. [Johns and Cunningham, 1983]

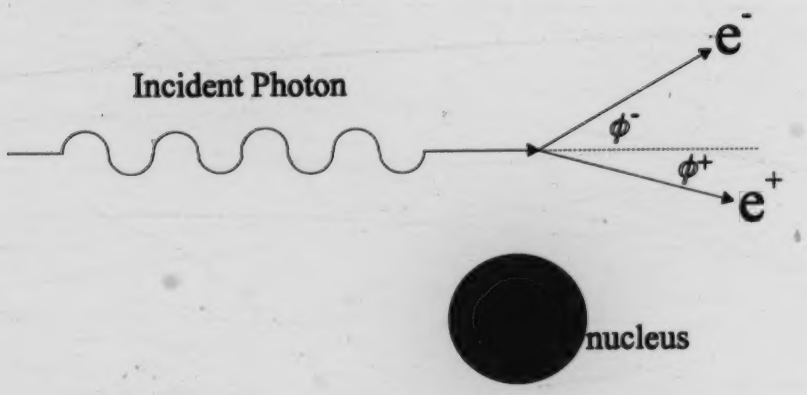

Figure: 2.5 Schematic of pair production. An incident photon, passing through the Coulomb force field of an atomic nucleus, vanishes giving rise to a positron-electron pair. [Attix, 1986]

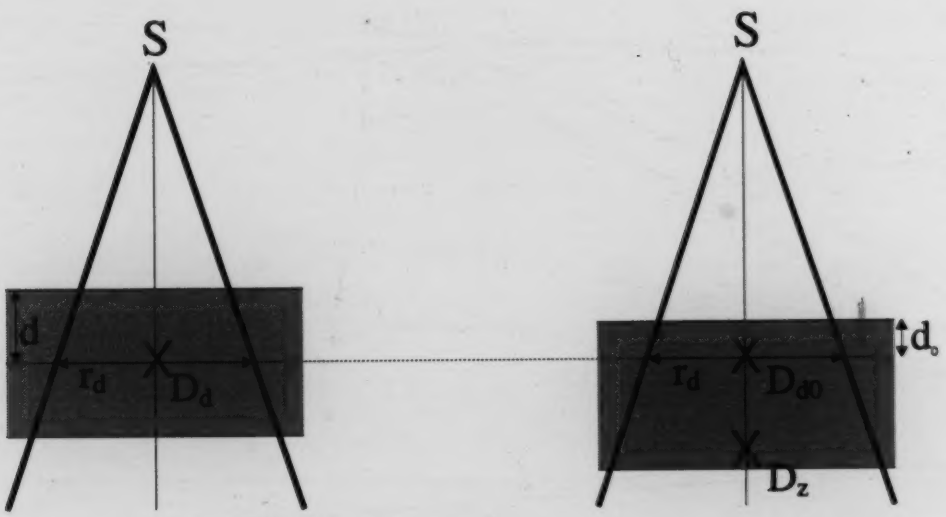

Figure 2.6: A diagram illustrating the definitions of the tissue-phantom ratio (TPR) and the percentage depth dose (PDD). $TPR(d,r_d)=D_d/D_{d0}$, where d_0 is the reference depth, S is the source, r_d is the field size at a depth d. $PDD = D_z/D_{d0} \times 100\%$ [adapted from Khan 1994].

Chapter 3

MRI Fricke Gel Dosimeter

As previously mentioned in Chapter 1, the MRI Fricke gel dosimeter combines a chemical dosimeter and a clinical MRI scanner. The chemical dosimeter used in this thesis is the Fricke solution dosimeter, first proposed by Fricke and Morse [1927], who observed that the extent of the chemical reaction was dependent on the amount of Roentgen rays that were delivered. When a ferrous sulphate solution is irradiated, ferrous (Fe^{2+}) ions are oxidized to ferric (Fe^{3+}) ions; this reaction will be described in Section 3.2. The extent of this chemical change was originally measured optically but can now be measured using MRI. If a three-dimensional or two-dimensional dose distribution is required, the Fricke solution is infused into a gelatin matrix and then imaged using MRI. In our study, we measured the relaxation rate of protons (spin 1/2) which gives information about the chemical properties of the solution.

There are two properties of an object that are probed by an NMR signal, referred to as relaxation rates: spin-lattice (R1) and spin-spin (R2) (See section 3.3). Ferrous and ferric ions, both paramagnetic species, have an influence on the relaxation rates of the proton signal in a Fricke gel. These influences are very different for the two species, thus allowing useful information to be gathered from the relaxation times of the protons [Bloembergen 1957]. The change in proton relaxation rates due to the formation of Fe^{3+} ions is related to the dose delivered to the system.

Some researchers have moved away from Fricke infused gels to a polymer gel known as BANG, which is an aqueous gel consisting of Bisacrylamide (Bis) and

Acrylamide monomers [Maryanski *et al.* 1993, 1994] that undergoes a chemical change due to irradiation. The chemical change involves the formation of cross-linked polyacrylamide. The presence of the polymer enhances the relaxation rate R2 of water, which is measured using MRI [Maryanski *et al.* 1993, 1994, Audet 1995]. The major difference in the BANG dosimeter as compared with the Fricke gelatin dosimeter is that the former results in a permanent representation of dose distributions that does not degrade over time, and also has a higher sensitivity. This feature allows for read out of the dose distribution at the user's convenience [Maryanski *et al.* 1996]. Unfortunately, these gels are more expensive and more difficult to prepare.

The rest of this chapter will focus on the development of the Fricke gel dosimeter over the past 13 years, and then go into the chemistry of the reaction as well as theory of NMR related to the dosimeter.

3.1 Development of the MRI Fricke Gel Dosimeter

In 1984, Gore *et. al.* [1984] realized that measuring chemical changes due to irradiation with magnetic resonance imaging could be exploited for dosimetry purposes. Their study demonstrated that there was a linear relationship between the relaxation rates R1 and R2, and dose for Fricke solution. In 1992, Podgorsak and Schreiner [1992] showed that the spin-lattice relaxation rate (R1) of liquid Fricke solution is linearly dependent on dose at low doses but saturates at about 400 Gy.

There are two types of gel matrices that are commonly used in combination with Fricke solution: agarose and gelatin. For this thesis we have chosen to use gelatin as it is easier to prepare and handle. Studies have shown that if the solution is incorporated into a gel matrix to reduce diffusion of the irradiated ions [Gore *et. al.* 1984], the dose response still exists and is more sensitive [Appleby *et. al.* 1988]. There also is the added advantage of producing high resolution spatial distributions of absorbed dose. The main limitation on spatial resolution is that of the MRI unit that

is utilized. Other gelling agents have also been used, including polyacrylamide [deGuzman *et al.* 1989] and a mixed polymer gel [Hiraoka *et al.* 1986, 1993], with results that did not provide any advantages over those of gelatin or agarose.

Most of the research presently being conducted on MRI Fricke gels use R1 as the indicator for dose [Appleby *et al.* 1987, Olsson *et al.* 1989, Schultz *et al.* 1990, Olsson *et al.* 1990, Hazle *et al.* 1991, Audet *et al.* 1993, Keller 1994, and Kron and Pope 1994], although research has indicated that spin-spin relaxation rate (R2) is a more sensitive measure [Prasad *et al.* 1991, Gambarini *et al.* 1994, Duzenli *et al.* 1994]. This thesis describes an investigation of the MRI Fricke gel dosimeter using R2 as the indicator of absorbed dose.

Appleby *et al.* [1988] determined that the dosimeter is independent of dose-rate in the range between 0.43 and 3.7 Gy min^{-1}. Shultz *et al.* [1990] found that the dosimeter was independent of dose rate in the range 4.7 to 24.2 Gy min^{-1}. For clinical purposes, the dose rate that is normally used is 2 - 4 Gy min^{-1} for high energy photons and electrons. Studies have shown that the sensitivity of the dosimeter increases slightly with increasing ferrous ion concentration in the range of 0.1 to 0.5 mM, but additional ferrous sulphate does not result in any further increase in sensitivity [Hazle *et al.* 1991, Shultz *et al.* 1990]. Duzenli *et al.* [1994] did extensive investigations of the effect of pH, gelatin concentration and the addition of organic impurities, and found that the most reliable composition of the gelatin dosimeter was 1 mM ferrous sulphate, 0.05 M sulphuric acid, and 4% gelatin by weight. The presence of sulphuric acid has two purposes: it provides an acid environment for the chemical reaction so as to provide H^+ ions required for the reaction, and its presence allows the dosimeter to behave like tissue [Fricke and Peterson 1927].

The effects of diffusion of the ferric and ferrous ions have been investigated by a number of researchers. Such diffusion causes a reduction in the quality of images obtained because of a loss of spatial resolution. Olsson *et al.* [1992] measured the diffusion constant of ferric ions to be $(1.91 \pm 0.09) \times 10^{-2}$ cm^2h^{-1}, and suggested that the images should therefore be taken within 2 hours of irradiation. This

experiment was performed using a dosimeter of composition: 1 mM $Fe(NH_4)_2(SO_4)_2$, 1.0 mM NaCl, 0.05 M H_2SO_4, 1.25% by weight SeaPlaque and 0.25% by weight SeaGel, which are types of agarose gel. A diaphragm diffusion cell was used to measure the diffusion constant at a temperature of 25 °C. This value is in fair agreement with the results obtained by Shultz *et al.* [1990], whose value was 1.58 x 10^{-2} cm^2h^{-1}, and by Kron *et al.* [1994], whose value was 2 x 10^{-2} cm^2h^{-1}. Schultz *et al.* [1990] obtained the diffusion coefficient by measuring the concentration of ferric ion that diffused from the surrounding solution into a petri dish containing 1% by weight of agarose gel. The concentration of the ion was measured using a NMR spectrometer. On the other hand, Kron *et al.* [1994] measured the diffusion constant by looking at the change in R1 across the junction of the two phases of an agarose gel (1.5% by weight). Balcom *et al.* [1995] looked at the diffusion of ferric ions from the surrounding solution into 1% by weight agarose gel, by measuring the change in ferric ion concentration using R1. They determined that the diffusion constant previously determined was incorrect, and should be taken to be (1.0 ± 0.1) x 10^{-2} cm^2h^{-1} at room temperature. New polymer gels, which do not rely on the Fricke solution but are related to absorbed dose by a cross-linking effect, have been proven to have no diffusion limitations [Maryanski *et al.* 1993, 1994].

The Fricke gel dosimeter can be used with electrons as well as photons. Olsson *et al.* [1990] conducted a study using a 14 MeV electron beam. The results of this experiment were that the depth dose curves and profiles measured using the MRI Fricke gel dosimeter were found to be in good agreement with diode measurements. The ability of the dosimeter to handle brachytherapy sources [Olsen *et al.* 1994, Parker *et al.* 1994, Duzenli 1995] was also investigated. The brachytherapy source used in all studies was the HDR Ir-192 source[2]. Olsen *et al.* [1994] also studied a low dose rate (LDR) ^{106}Ru source as well as the HDR ^{192}Ir source, and found satisfactory results for both cases.

---

[2] Nucletron Corporation, Veemendaal, The Netherlands

An important question is whether the Fricke gel dosimeter is capable of integrating a time dependent radiation field such as would be created by a dynamic wedge. A wedge is a filter that modifies the beam's isodose distribution by causing a progressive decrease in the intensity across the beam. Most wedges are tapered blocks that are placed in the path of the beam, but a dynamic wedge is created when collimators move across the beam during delivery, causing the same effects as a stationary wedge. Bengtsson *et. al.* [1996] found that the dosimeter could handle dynamic wedges quite effectively.

3.2 Radiation Chemistry of the Fricke Dosimeter

The net reaction is the oxidization of ferrous ions to ferric ions, brought about by the indirect effects of radiation via free radical intermediates, for example H and OH, that are formed during the radiolysis of water. The entire oxidation reaction is summarized in the following main equations [Fricke and Hart 1966]:

$$\begin{aligned} &Fe^{2+} + OH \rightarrow Fe^{3+} + OH^- \\ &H + O_2 \rightarrow HO_2 \\ &Fe^{2+} + HO_2 \rightarrow Fe^{3+} + HO_2^- \\ &HO_2^- + H^+ \rightarrow H_2O_2 \\ &Fe^{2+} + H_2O_2 \rightarrow Fe^{3+} + OH + OH^- . \end{aligned} \tag{3.1}$$

The above reactions are heavily dependent on the initial concentrations of oxygen and ferrous ions and their response is linear in the region 40 Gy to 400 Gy. Above 400 Gy, the response saturates due to depletion of oxygen or depletion of ferrous ions, or both. To extend the range in either direction a number of suggestion have been put forward. When using optical measuring devices, the lower limit is governed by the size of the absorption cell used. By increasing the length of the cell to 10 cm, the dose can be measured down to 4 Gy [Fricke and Hart 1966]. This corresponds also to

the minimum detectable dose when using R1 as a measure [Podgorsak and Schreiner 1992]. The reactions in (3.1) are also dependent on temperature and pH.

The chemical yield of ferric ions is described by the G-value, which is the number of molecules of product produced per 100 eV of absorbed energy. The dose, D, is related to chemical yield through the following relationship:

$$D = \frac{\Delta M}{G\rho} \times 9.65 \times 10^{7} \text{ Gy}, \tag{3.2}$$

where ΔM is the concentration of ferric ions produced in moles L^{-1}, and ρ is the density of the ferrous sulphate solution in kg m^{-3} [Fricke and Hart 1966]. The net yield of ferric ions can be written in terms of the G-values of the radicals responsible for their production:

$$G\left(Fe^{3+}\right) = 2G_{H_2O_2} + 3G_H + G_{OH}. \tag{3.3}$$

For the standard Fricke solution, 1 mM $FeSO_4$ and 0.8 N H_2SO_4, the G-value of Fe^{3+} is 15.5 ions $(100 \text{ eV})^{-1}$ [Swallow 1973]. For the MRI Fricke gel dosimeter, where gelatin was the gelling agent, the G-value was determined to be 42 ± 1 $(100 \text{ eV})^{-1}$ [Duzenli 1995].

3.3 NMR Theory of the Fricke Gel Dosimeter

Many atomic nuclei possess non-zero spin, and hence a non-zero magnetic moment which arises because of circulating currents within the nucleus. The magnetic moment, μ, of the nucleus is related to the spin angular momentum, **I**, by the following relationship:

$$\mu = \gamma \mathbf{I}, \tag{3.4}$$

where γ is called the gyromagnetic ratio. Quantum mechanical treatment shows that the magnitude of the angular momentum vector is $\sqrt{(I(I+1))}\,\hbar$, where the spin number I takes integral or half integral values. The z component of the angular momentum vector is $m\hbar$ where m takes the values I, (I-1), ..., -I. It follows that the angular momentum vector possesses transverse components I_x and I_y in addition to the longitudinal component I_z. For protons, I = ½, the possible values of m are ± 1/2 and γ is measured to be $2.675 \times 10^8\ s^{-1}\ T^{-1}$ [Morris 1986].

In the presence of an external magnetic field, each nucleus will experience a torque causing it to precess around the magnetic field at a frequency known as the Larmor frequency, ω_0, which is proportional to the magnetic field strength, B_0, and is given by:

$$\omega_0 = \gamma B_0. \tag{3.5}$$

If an external magnetic field, taken to be in the z direction, is applied to a system of hydrogen nuclei, the z component of their magnetic moments will align either parallel or anti-parallel to the field. According to the Maxwell-Boltzman distribution, the probability of a nucleus being in a state with energy E, at a temperature T, is

proportional to $e^{-E/kT}$. Thus the ratio of the populations of the anti-parallel (higher energy) states to the parallel (lower energy) states, N^- and N^+ respectively, is given by:

$$\frac{N^-}{N^+} = e^{\frac{-\hbar\omega_0}{kT}}, \tag{3.6}$$

where $\hbar\omega_0$ is the energy difference of the two states. In thermal equilibrium, the net magnetization vector $\mathbf{M}_0$ of the system is parallel to the magnetic field and is calculated by adding up all the parallel magnetic moments and then subtracting the anti-parallel moments.

In an NMR experiment, $\mathbf{M}_0$ is perturbed by applying an alternating radiofrequency (rf) magnetic field $\mathbf{B}_1$, which is perpendicular to $\mathbf{B}_0$. In the absence of other interactions, the magnetization vector $\mathbf{M}_0$ will precess around $\mathbf{B}_1$ in the rotating frame, i.e. a frame of reference rotating around $\mathbf{B}_0$ at a frequency ω_0. If the rf field is turned off after $\mathbf{M}_0$ has precessed through 90°, as shown in Figure 3.1a, the magnetization vector is located in the transverse plane and this pulsed rf field is called a 90° pulse. If the rf field is turned off after $\mathbf{M}_0$ has precessed through 180°, as shown in Figure 3.1b, the magnetization vector is reversed and this pulsed rf field is called a 180° pulse [Morris 1986].

Eventually the magnetization vector will return to its equilibrium state where it is parallel to the magnetic field. The process by which this occurs is described as relaxation. In the process of relaxation, energy is given up either to the surrounding lattice, by spin-lattice relaxation, or to another spin, by spin-spin relaxation. The recovery of the z component of the magnetization vector, M_z, following a 90° pulse is given by:

$$\mathbf{M}_z = \mathbf{M}_0\left(1 - e^{\frac{-t}{T1}}\right), \tag{3.7}$$

where T1 is known as the spin-lattice relaxation time. Thus T1 is the time taken by the magnetization vector to return to 63% of its original value following a 90° pulse. The recovery of the z component of the magnetization vector, Mz, following a 180° pulse is given by:

$$M_z = M_0\left(1-2e^{\frac{-t}{T1}}\right), \tag{3.8}$$

The recovery of a transverse component of the magnetization vector, M_x, following a 90° pulse is given by:

$$M_x = (M_x)_0 e^{\frac{-t}{T2}}. \tag{3.9}$$

where $(M_x)_0$ is the transverse component at time zero and T2 is known as the spin-spin or transverse relaxation time. Thus T2 is the time required for the transverse component of M to decay to 37% of its initial value [Morris 1986].

The relaxation rate R1, defined as 1/T1, and the relaxation rate R2, defined as 1/T2, have both been used as an indicator of the radiation dose delivered to the Fricke gel system [Gore *et al.* 1984]. Since this thesis deals with the response of R2 to absorbed dose, a more detailed description of the spin-spin relaxation process is given in the next section.

3.3.1 Spin-Spin Relaxation

Spin-spin relaxation is a result of energy being transferred between spins as the transverse magnetization M_{xy} decays to its equilibrium value of zero. In a system

of two spin 1/2 particles, **I** and **S**, there are four eigenstates for the unperturbed Hamiltonian. These eigenstates are obtained from:

$$I_{x,y}|\alpha\rangle, \qquad I_{x,y}|\beta\rangle, \qquad S_{x,y}|\alpha\rangle, \qquad S_{x,y}|\beta\rangle, \tag{3.10}$$

and are designated as:

$$|\alpha\alpha\rangle, \qquad |\beta\beta\rangle, \qquad |\alpha\beta\rangle, \qquad |\beta\alpha\rangle, \tag{3.11}$$

where $|\alpha\rangle$ and $|\beta\rangle$ are states corresponding to m = 1/2 and m = -1/2, respectively. These four states of the spins are not eigenstates of energy but rather those of the components of the spin operators [Solomon 1955]. These states are orthogonal and can be depicted as in Figure 3.2 if the two spins are alike. The transition probabilities per unit time, U_0, U_1, U_1', and U_2 between these states can be calculated for a particular Hamiltonian, $\mathcal{H}$, by the relation

$$U_{ab} = \frac{1}{\hbar^2}\left|\int_{-\infty}^{+\infty}\sum_{ij}\langle m_i|\mathcal{H}|m_j\rangle a_i b_j e^{-i\omega_{ij}t'}\,dt'\right|^2, \tag{3.12}$$

where a_i and b_i are obtained from the following relations when looking at two orthogonal states $|a\rangle$ and $|b\rangle$

$$|a\rangle = \Sigma_i a_i|m_i\rangle, \tag{3.13a}$$

$$|b\rangle = \Sigma_j b_j|m_j\rangle. \tag{3.13b}$$

For systems where the two spins, **I** and **S**, are alike, i.e. $\gamma_I = \gamma_S$, as assumed above, the transverse relaxation rate is given by

$$R2 = 2(U_1 + U_2). \tag{3.14}$$

If the spins **I** and **S** are different, for example when **I** is a spin 1/2 nucleus and the spin **S** is a paramagnetic ion in solution, the transverse relaxation rate for the nuclear spin is given by

$$R2 = (U_0 + 2U_1 + U_2). \tag{3.15}$$

For a two spin system there are two main interactions, the dipole-dipole interaction and the so-called contact term of the hyperfine interaction. The dipole-dipole and hyperfine terms are considered to be perturbations of the main Zeeman Hamiltonian $\mathcal{H} = -\boldsymbol{\mu} \cdot \mathbf{B}$. The dipole-dipole Hamiltonian, $\mathcal{H}_D$, is given by:

$$\mathcal{H}_D = \frac{\mu_0}{4\pi r^3}\left[\boldsymbol{\mu}_I \cdot \boldsymbol{\mu}_S - 3(\boldsymbol{\mu}_I \cdot \hat{\mathbf{r}})(\boldsymbol{\mu}_S \cdot \hat{\mathbf{r}})\right], \tag{3.16}$$

where μ_0 is the permittivity of free space, $\hat{\mathbf{r}}$ is the unit vector joining the two spins, and $\boldsymbol{\mu}_I$ and $\boldsymbol{\mu}_S$ are the magnetic moments of the two spins **I** and **S**, respectively. The Hamiltonian of the contact term of the hyperfine interaction, $\mathcal{H}_C$, is given by:

$$\mathcal{H}_C = \hbar A \mathbf{I} \cdot \mathbf{S}, \tag{3.17}$$

where A is the coupling constant and is a measure of the strength of the hyperfine interaction [Solomon 1955].

The relaxation rate in the case of the dipole-dipole interaction, $R2_D$, is given by:

$$R2_D = \frac{S(S+1)\hbar^2\gamma_I^2\gamma_S^2}{15r^6}\left[4\tau_c + \frac{3\tau_c}{1+\omega_I^2\tau_c^2} + \frac{13\tau_c}{1+\omega_S^2\tau_c^2}\right], \quad (3.18)$$

where r is the distance between the nuclear and paramagnetic ion spins **I** and **S**, S is the spin number of spin **S**, and τ_c is the correlation time of the interaction [Koenig and Brown 1984]. The ion-water distances in aqueous solutions for ferrous and ferric ions are 0.212 nm and 0.203 nm, respectively [Marcus 1983]. For the ferrous and ferric ions, γ_S is taken to be 658 times γ_I due to the ratio of electric charge to mass [Gore *et al.* 1984]. The dipolar correlation times are taken to be 5.1 x 10^{-11} s and 1.5 x 10^{-12} s, for Fe3+ and Fe2+, respectively [Eisinger et al. 1962]. The relaxation rate, $R2_C$, for the contact term is given by:

$$R2_C = \frac{A^2}{3\hbar^2}S(S+1)\left[\frac{\tau'_c}{1+\omega_S^2\tau'^2_c} + \tau'_c\right]. \quad (3.19)$$

where τ_c' is the correlation time of the interaction [Koenig and Brown 1984] and $A/\hbar$ = 1.2 x 10^7 s^{-1} [Luz and Shulman 1965].

The dipole-dipole interaction correlation time, τ_c, results from three independent processes: relative rotation of the two spins (τ_r), proton exchange (τ_h), and electron spin relaxation (τ_e) and can be written as:

$$\frac{1}{\tau_c} = \frac{1}{\tau_r} + \frac{1}{\tau_h} + \frac{1}{\tau_e} \approx \frac{1}{\tau_r} + \frac{1}{\tau_e}, \quad (3.20)$$

since τ_h in water is known to be very long and is usually neglected [Gore *et al.* 1984]. The contact interaction correlation time, τ_c', is only a function of proton exchange (τ_h) and electron spin relaxation (τ_e). Therefore since $1/\tau_h$ is usually neglected, $\tau_c'=\tau_e$.

For more information, a full quantum mechanical description of spin-spin relaxation in a system of two spins can be found in the literature [Solomon 1955].

3.3.2 Relaxation Effects due to Paramagnetic Ions

Bloembergen *et al.* [1948] noticed that water with dissolved paramagnetic ions behaved differently than pure water. The relaxation time of protons in water is approximately two seconds [Bloembergen *et al.* 1948], but with added paramagnetic ions, the relaxation time is greatly reduced by up to five orders of magnitude [Koenig and Brown 1984]. The relaxation of protons in the presence of paramagnetic ions is dominated by the interactions between the electronic spins and the spins of the protons. The spin-spin relaxation rate, including both the dipolar and contact terms, for protons hydrating paramagnetic ions is given by

$$R2_M \approx \frac{S(S+1)\hbar^2\gamma_S^2\gamma_I^2}{15r^6}\left[4\tau_c + \frac{3\tau_c}{1+\omega_I^2\tau_c^2} + \frac{13\tau_c}{1+\omega_S^2\tau_c^2}\right] + \frac{1}{3}\frac{S(S+1)A^2}{\hbar^2}\left[\tau_e + \frac{\tau_e}{1+\omega_S^2\tau_e^2}\right], \tag{3.21}$$

where τ_e is the electron spin relaxation time, which is dependent on the magnetic field strength and the type of paramagnetic species, and can be written in the form:

$$\tau_e = \tau_{e0}\left(1+\omega_S^2\tau_v^2\right). \tag{3.22}$$

Here, τ_v is a frequency independent parameter, typically ~10^{-11} s, and τ_{e0} is the electron spin relaxation time at zero frequency, determined to be 6.94 x 10^{-10} s [Koenig and Brown 1984].

3.4 NMR Dosimetry of the Fricke Dosimeter

In Section 3.3.2, a discussion of the spin-spin relaxation rate of protons in water hydrating paramagnetic ions was presented, but in the case of the Fricke gel dosimeter there are other sites for proton relaxation that have to be considered. These sites include the bulk water protons and protons in water hydrating the macromolecules of the gelling agent. Therefore, the Fricke gels provide four environments between which the water protons may migrate. If there exists a fast exchange between these environments, the spin system decays exponentially with a single rate which is the weighted sum of the inherent relaxation rates in each environment [Schreiner *et al.* 1991]. Therefore, the overall relaxation rate, R2, in a Fricke gel is given by:

$$R2 = \frac{1}{T2} = f_w \frac{1}{T2_w} + f_g \frac{1}{T2_g} + f_{2+} \frac{1}{(T2_M)_{2+}} + f_{3+} \frac{1}{(T2_M)_{3+}}, \qquad (3.23)$$

where the subscripts w and g refer to bulk water and gel respectively. The factors f_{3+} and f_{2+} are given by

$$f_{2,3+} = q \frac{[Fe^{2,3+}]}{[H_2O]}, \qquad (3.24)$$

where q is the water co-ordination of the ion, representing the number of water molecules in direct contact with the ion, and is taken to be 6 for ferric and ferrous ions [Koenig and Brown 1984]. The molarity of water [H_2O] is 55.6 moles L^{-1}.

Relaxivity, $\Re 2$, is defined as the change in spin-spin relaxation rate per mM of a particular paramagnetic ion, and is therefore given by

$$\Re 2 = \frac{6\times10^{-3}}{55.6}\left[R2_M\right]. \tag{3.24}$$

Due to the fact that $R2_M$ increases linearly with increasing paramagnetic ion concentration, the term relaxivity was coined to describe relaxation without the dependence of concentration. In the Fricke gelatin system, the change in relaxivity is the measure of the radiation dose experienced by the system. Equation 3.2 can be re-written to reflect what is measured using NMR:

$$\delta R2 = 1.037\text{x}10^{-10} DG\rho\left(\Re 2_b - \Re 2_a\right), \tag{3.25}$$

where $\delta R2$ is the change in relaxation rate due to irradiation, and the subscripts *a* and *b* denote the relaxivities due to the ferrous ion and the ferric ion respectively [Gore *et al.* 1984].

3.5 Magnetic Resonance Imaging

3.5.1 The Spin-Echo Sequence

To quantify spin-spin relaxation and obtain the time constant T2, the spin-echo sequence is used. This sequence was first devised by Hahn [1950] who realised that the time constant of the decay of the signal after a single 90° pulse was applied was not the true T2 of the sample. This is because the transverse signal, which was obtained by tipping the magnetization vector into the transverse plane by the 90° pulse, begins to decay and dephase due to local variations in the magnetic field, more specifically B_0 inhomogeneities. In many cases this decay is approximately exponential and the associated time constant is called T_2^*. Therefore, Hahn [1950] devised a method of measuring the true decay of the transverse magnetization by

applying another 90° pulse at a specified time after the first 90° pulse. The effect of this second pulse is to rephase the signal and once rephasing is complete, an echo is produced whose amplitude gives an approximate representation of the true T2 decay of the sample. The time between the first 90° pulse and the second 90° pulse is known as τ and the echo appears at a time 2τ after the first 90° pulse, which is also known as TE. A number of Hahn echoes are required to sample the T2 decay curve. This is accomplished by varying the time τ and then measuring the amplitude of each echo. This technique is time consuming and suffers from the disadvantage that some signal is lost because the magnetization is rotated into the z direction.

A better way of determining T2 is to apply a 180° pulse instead of a 90° pulse at a specific time after the initial 90° pulse, this being called a spin-echo pulse sequence. In this case, no signal is lost by the magnetization vector being transferred into the z direction. Carr and Purcell [1954] later modified this spin-echo sequence to include a train of 180° pulses instead of one 180° pulse, as shown in Figure 3.3, in order to speed up data acquisition. Each 180° pulse was applied a time TE apart, thereby allowing for sampling of the T2 decay curve with just one initial 90° pulse. This provided more accurate estimations of T2. Unfortunately, this pulse sequence also encounters drawbacks due to non-uniform 180° pulses, and therefore Meiboom and Gill [1958] suggested applying the 90° pulse and the 180° pulse orthogonal to one another. With both of the modifications suggested, the entire sequence is known as the CPMG multi-echo sequence. Another modification that is sometimes applied when using a CPMG sequence is to alternate the phase of the 180° pulse by 180°, that is, apply a +180° pulse, then a -180° pulse, and repeat this alternating pattern for the number of signal averages required. This modified CPMG sequence is known as the phase alternated CPMG.

The amplitude of the echoes created in the CPMG sequence are dependent on a number of parameters which include the proton density of the sample, ρ, the timing parameters, T1, T2 and the gain of the MRI receiving instrumentation, k. The signal

amplitude for echo number n of N echoes obtained from a CPMG sequence can be written as:

$$S(n, T1, T2, \rho, TE, TR) = k\rho\left[1 - 2e^{-\left(\frac{(TR-(N-1/2)TE)}{T1}\right)}\right]e^{-\left(\frac{TR-(N-1)TE}{T1}\right)}e^{-\left(\frac{nTE}{T2}\right)}, \quad (3.26)$$

[Dixon and Ekstrand 1982]. Long repetition times, TR, values are used in the measurement of T2 to reduce the influence of T1 on the measurements.

3.5.2 Standard Imaging Protocol

To obtain images, additional static magnetic fields known as gradient fields are used. These gradient fields vary linearly in magnitude along three Cartesian axes and are created by electric currents in specially shaped coils wound around a tube in the bore of the magnet. These gradients are used to spatially encode nuclear spins in the volume of interest. However, it is easier to obtain information about a three-dimensional volume by taking several two-dimensional slices and reconstructing the volume afterwards.

In order to image a slice, it is necessary to use a soft 90° pulse in combination with a gradient, G-slice, applied in a direction perpendicular to the slice. A soft pulse is one in which the amplitude is modulated so that only spins in a defined frequency (spatial) region are excited. The thickness of the slice is inversely proportional to the amplitude of the gradient. The negative lobe of the G-slice gradient is the same amplitude as the positive lobe but half its duration, as shown in Figure 3.4, and serves to rephase the transverse magnetization arising from different depths in the slice. To spatially encode the other two directions, gradients known as frequency and phase encoding gradients are used. The frequency encoding gradient, G-freq, is applied

during the read-out or acquisition of the signal. This gradient provides a measure of nuclear density as a function of frequency. By applying a linear gradient, each nucleus will possess a different local "frequency" which will then correspond to a certain "plane" perpendicular to G-freq. The negative lobe of G-freq, which is the same amplitude but half the duration of the positive lobe, is called the dephasing lobe. This lobe ensures that perfect refocusing of both the B_0 inhomogeneity and the G-freq gradient will occur at the same instant. As can be seen in Figure 3.4, the phase encoding gradient, G-phase, is applied during the time between the 90° pulse and the 180° pulse. By the end of the gradient pulse, the nuclear spins will have accumulated different phase angles depending upon their spatial location in the direction of the phase encoding gradient. To extract such spatial information, the imaging sequence is repeated several times while incrementing the amplitude of the phase encoding gradient.

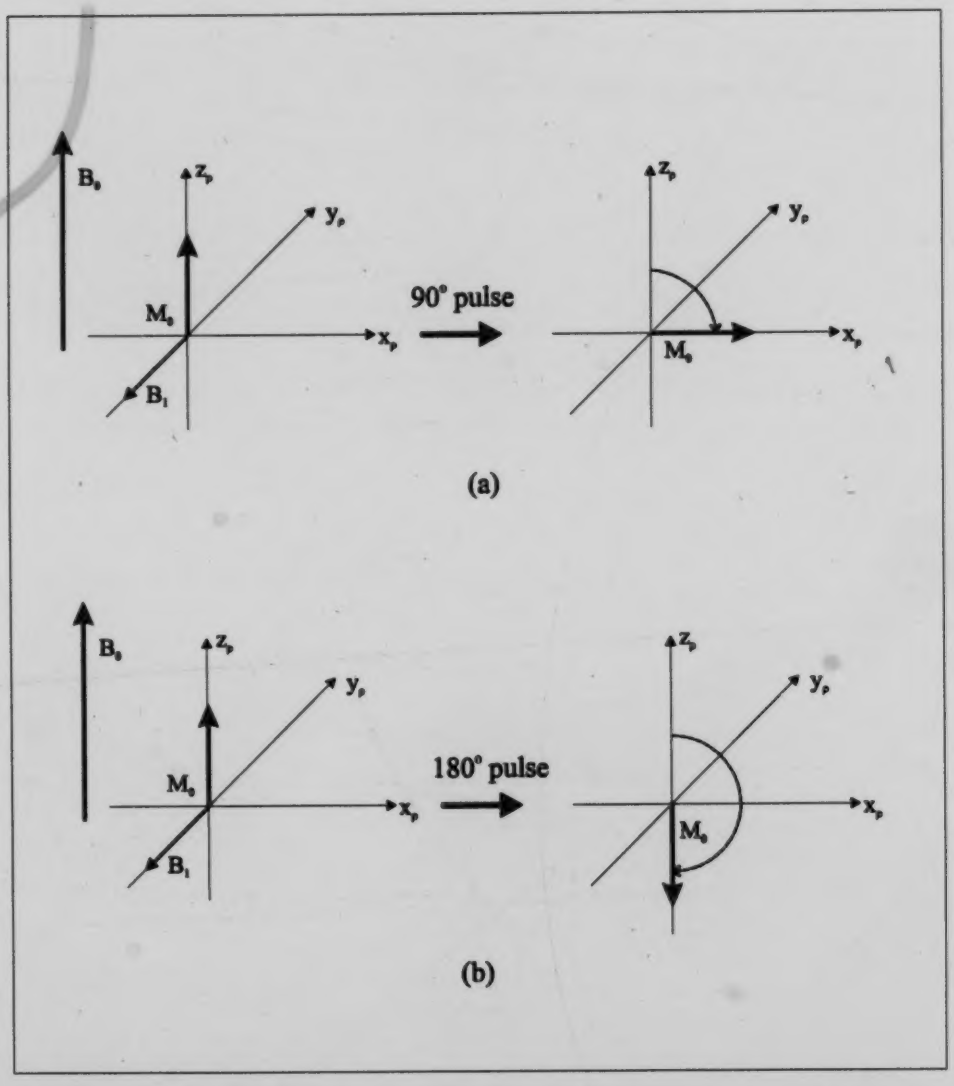

Figure 3.1: Effect of a rf pulse in the rotating frame of reference ($x_\rho y_\rho z_\rho$), where (a) the pulse is a 90° pulse and (b) the pulse is a 180° pulse. In both cases the pulse is directed along the $-y_\rho$ axis.

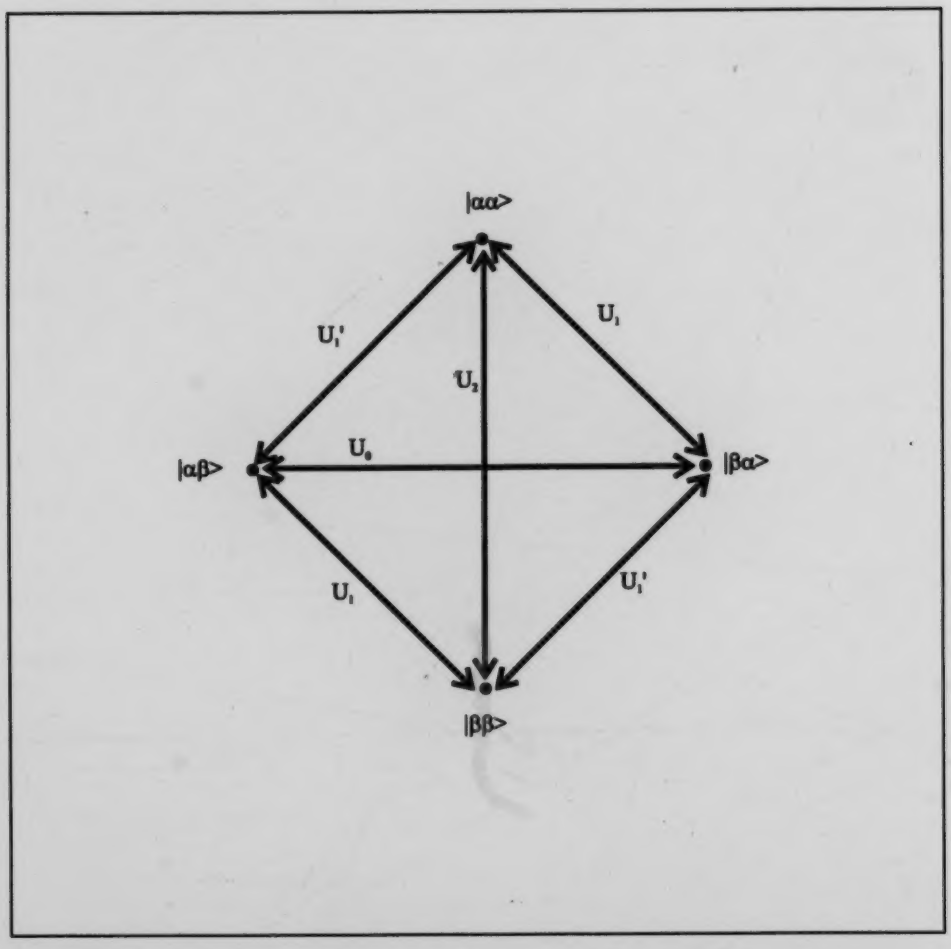

Figure 3.2: Transition probabilities between the eigenstates of the transverse components of the spin operator for a system of two like nulcei [adapted from Solomon 1955].

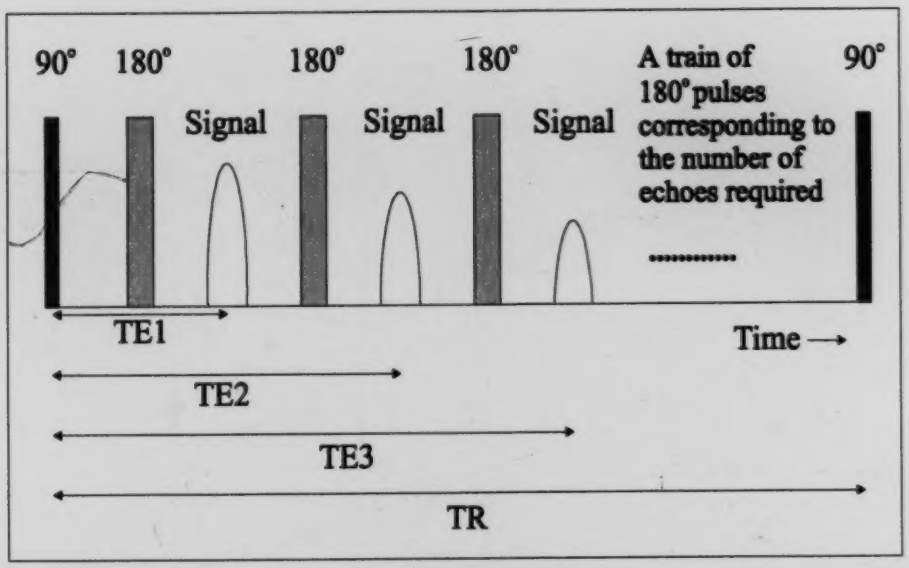

Figure 3.3: A spin-echo sequence showing the first 90° pulse followed by a train of equally spaced 180° pulses.

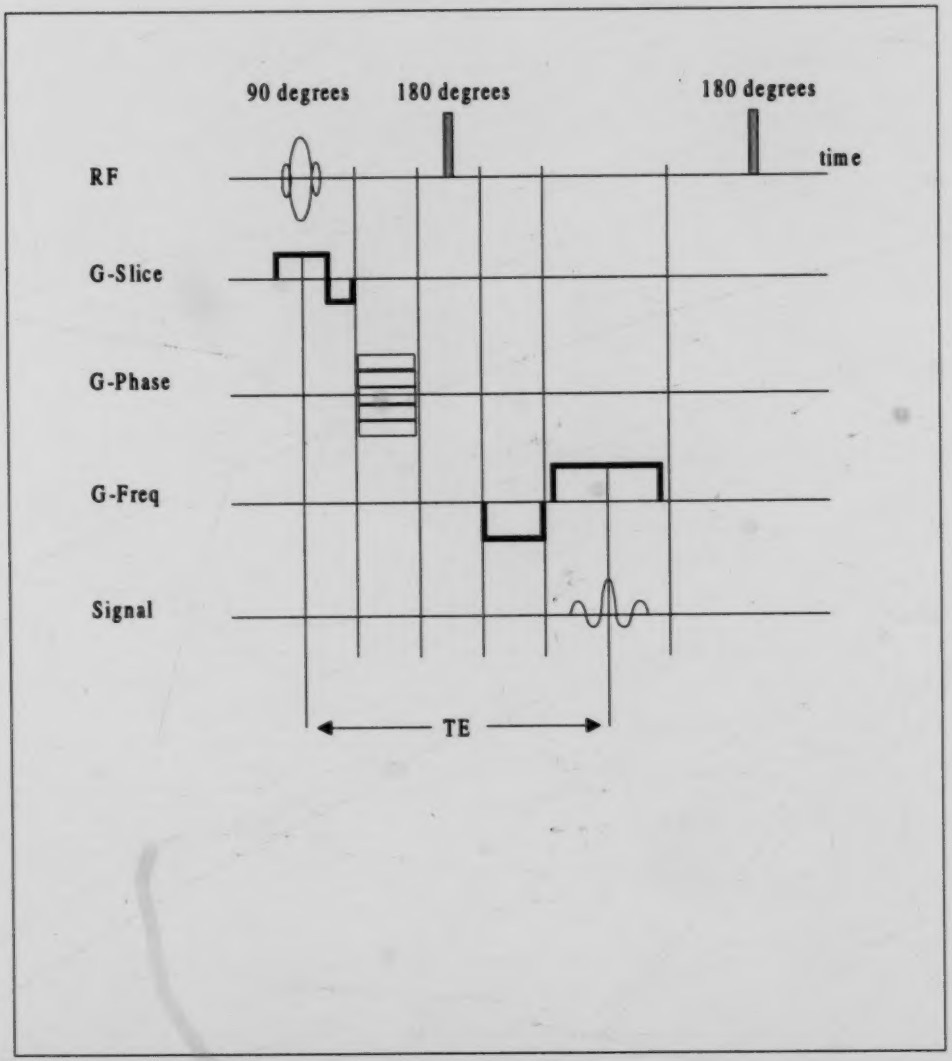

Figure 3.4: A timing diagram showing the rf pulses and gradients used in the spatial encoding of images acquired in a spin-echo sequence.

Chapter 4

Materials and Methods

4.1 Sample Preparation

The Fricke-gelatin composition used in this thesis is 0.05 M sulphuric acid, 4% gelatin by weight and 1 mM ferrous sulphate. No sodium chloride or any organic compounds were added. The gel used was 300 bloom swine skin gelatin. Preparation involved soaking the required mass of gelatin, approximately 80 g for a 2L phantom, in about 50% of the final volume for approximately 20 minutes. The gelatin mixture was then heated in a microwave oven for approximately 5 minutes on medium high, stirring once after the first 3 minutes. Warm distilled water was then added to the gelatin until 75% of the final volume was reached. For the ferrous sulphate solution with sulphuric acid, 20% of the final volume was measured out and the required mass of ferrous sulphate and volume of sulphuric acid were added. Distilled water was then added until 25% of the final volume of the phantom was measured. Warm ferrous sulphate solution was added to the melted gelatin. The Fricke-gelatin mixture was then poured into either a 2 L container or several 50 ml containers. The gel phantoms were allowed to cool and set in a dark cupboard before imaging and irradiation. The gelling procedure took at least 24 hours, so the imaging and irradiation usually took place approximately 48 hours after preparation. This is because there is a small shelf life of the gels and the gel matrix begins to degrade losing its structure after about 3 - 4 days after preparation. Therefore, irradiation and imaging should be done at the very latest 48 hours after preparation.

The two main phantom sizes used were a 15 cm diameter circular container and a 70 mm square bottle; both containers are made of plastic (polyethelyne). The circular container has a wall thickness of 0.86 mm while the square container has a wall thickness of 1.52 mm. For some of the electron studies, a third container was used which was box-shaped in shape. The dimensions of the latter are 12.9 cm x 11.2 cm and 18.0 cm high with a wall thickness of approximately 2 mm.

4.2 Irradiation

For the photon and electron studies, the phantoms were irradiated using a Clinac[3] 2300CD radiotherapy unit in the Department of Medical Physics at the Cross Cancer Institute (CCI). For the photon studies, samples were placed in a water tank, whose dimensions were 32.1 cm x 32.1 cm and 18.8 cm high with a wall thickness of 11.5 mm (13 mm effective water distance), to ensure full scatter. Beam energies of 6 MV and 15 MV were used. A field size of 15 x 15 cm^2 and a SSD of 91 cm was used for the circular phantom while a 10 x 10 cm^2 field size and 95 cm SSD was used for the square container. These SSDs were determined by assuming that the centre of the phantom would lie 100 cm way from the source and this centre point would act as the centre of rotation. For example, the square phantom was 74 mm wide at the centre due to slight bulging, and there was 26 mm of effective wall thickness of the tank for a total of 100 mm. Now divide 100 mm by 2, for the midpoint, gives 50 mm or 5 cm, therefore the SSD to the tank surface should be set to 95 cm. For the majority of the photon beam studies, the phantoms were irradiated to a uniform dose using parallel opposed beams. This irradiation technique was used to eliminate ion diffusion effects arising from dose gradients. The irradiation set-up that was used is depicted in Figure 4.1. After the first beam is applied the phantom is rotated 180° and the second beam is applied. Also one experiment was conducted at a beam energy of 200 kV, using a

[3] Varian Oncology Systems

Philips RT250 machine. For this low energy beam experiment only one beam, therefore no 180° rotation, was used due to the long irradiation times. For the electron studies, only a single beam was used with beam energies of 9, 12 and 18 MeV. The electron beam experiments were performed with a field size of either 4 x 4 cm^2 or 4 x 5 cm^2.

For the brachytherapy studies, the circular phantoms were used. These were irradiated with an Ir-192 brachytherapy source using a microSelectron[4] HDR brachytherapy unit also situated at the Cross Cancer Institute. The Ir-192 source has a complicated γ–ray decay scheme and an average photon energy of 0.38 MeV. The half life of the isotope is 74.2 days [Khan 1994]. The source was loaded into the phantom through a catheter whose inner and outer diameters were 1.5 mm and 2 mm, respectively. This process of auto-loading the source after the catheters are in place is known as remote afterloading [Nag 1994].

4.3 Imaging and Measurement of Dose Distributions

The imaging unit used in this thesis was the clinical MRI scanner[5] located at the CCI which operates at a frequency of 64 MHz, corresponding to a field strength of 1.5 Tesla. The pulse program used was the standard multi-echo phase-alternated CPMG sequence. Eight echoes were collected with two signal averages where the echo time, TE, was 50 ms and the repetition time, TR, was 2000 ms. Imaging was done in the *xy*-plane containing the beam axis for the photon studies, as shown in Figure 4.2, which was the coronal imaging plane as shown in Figure 4.3. Images were collected before and after irradiation and then were transferred to a UNIX system for analysis.

---

[4] Nucletron Corporation
[5] Philips Gyroscan

4.3.1 Phantom Positioning and Temperature Considerations

Positioning of the phantom for imaging purposes is especially important in this analysis because of the echo-quotient technique, which will be described in Section 4.3.2. If the phantom position has changed between pre- and post-irradiation imaging, that would lead to distortions that are seen especially at the edges of the phantom. To minimise such distortions, each phantom was located in a styrofoam block which conformed to its shape. Each styrofoam block was shaped to fit snugly in the MRI head coil. The phantom was positioned with its centre at the isocentre (position 0 on the bed position display) of the magnet using lasers and the auto isocentre bed motion control button. To guarantee that the position of the phantom inside the magnet is the same for pre- and post-irradiation, the bed was returned to position 0 without resetting the position of the lasers on the phantom. This ensured that the effects due to non-uniform tip angles were repeated so that the echo-quotient technique could be applied.

These gel phantoms need to be kept in a dark environment to reduce the possibility of spontaneous oxidation of the ferrous ions. The temperature of the phantom was allowed to equilibrate to room temperature (22 °C). There had been speculation that the temperature of the phantom might rise due to rf heating during imaging as well as due to heat transfer from the surroundings [Duzenli 1995] which would lead to changes in the T2 values. According to Duzenli [1995], a 1 °C variation in temperature would lead to a 1% change in R2. Experiments were performed to investigate the possibility of heating in phantoms. Two experimental set-ups were used, one where the phantom was fully enclosed and one where the phantom was half enclosed in styrofoam to reduce the heat exchange between the room and the phantom. The styrofoam was also used in ensuring accurate positioning as was described in the previous paragraph. The temperature in the bore of the magnet was found to be 23 °C whereas that of the console room was found to be 20°C, which is where the phantoms were kept. Because the temperature of the

console room was lower than the initial gel temperature of 22 °C, the temperature in some of the phantoms was found to be 21 °C before imaging was performed. However, the results indicated that there was no temperature rise in the phantom due to imaging.

4.3.2 Obtaining ΔR2 Images

Many studies have indicated that accurate estimates of T2 with clinical scanners are difficult to obtain due to non-uniform tip angles associated with an inhomogeneous rf field. This can be caused by imperfections in the design of the rf coil and by skin depth effects in large phantoms which have a high electrical conductivity, as in the case of the Fricke-gel dosimeter [Maryanski and Gore 1992]. These non-uniform tip angles produce stimulated echoes that appear as an artefact in the images, thereby introducing errors in values of T2 [Zur *et al.* 1987, Majumdar *et al.* 1986, Crawley and Henkleman 1987, Fransson *et al.* 1993]. This is more of a problem for imaging than spectroscopy because of the larger sample volumes that are used for imaging. Duzenli and Robinson [1995] postulated that taking the ratio of the images obtained before and after irradiation would reduce the error in the estimation of R2 and provide a more accurate measure of absorbed dose in the system. The parameter that is derived is known as ΔR2, the difference between the two R2 images. The reasoning is that any errors occurring during imaging would be the same before and after irradiation and therefore would cancel out when the ratio was taken. An expression for the amplitude of the echo signal, that emphasizes the R2 dependence is:

$$S(n) = f(n,x,y,z) \cdot k \cdot \rho \cdot P_1(T1,n,TE,TR) e^{-R2nTE}, \qquad (4.4)$$

where the function f(n,x,y,z) contains the imperfections due to the non-uniform tip angles. This function may also have a T1 and T2 dependence [Hughes 1977] but it is not significant because the dominant stimulated echoes have been removed [Duzenli 1995]. If this function, f(n,x,y,z), is constant for every image acquired for a particular sample, then it can be factored out by taking the ratio of the signal amplitude S′ (n), after irradiation, to S(n), before irradiation:

$$\frac{S'(n)}{S(n)} = \frac{P_1'(T1,n,TE,TR)}{P_1(T1,n,TE,TR)} e^{-(nTE(R2'-R2))} = A_n e^{-(nDR2)}. \qquad (4.5)$$

Duzenli [1995] found that this function, f, was reproducible for two separate scans and therefore could be considered to be constant. So for each pixel in the acquired scan matrix, a two parameter exponential fit to the above equation was performed, the two parameters being the amplitude, A_n, and the decay constant. The resultant decay constant extracted was ΔR2, which equals R2′-R2 (after-before). Therefore, instead of an R2 image, a ΔR2 image is produced. This analysis is known as the echo-quotient technique.

To determine the decay of the signal and thus ΔR2, a fit to the data must be performed. There are many ways one could perform this fit. The method that was chosen was the Marquardt algorithm, a nonlinear least-squares routine. The Marquardt algorithm takes a set of data points and their associated standard deviations and fits them to a non-linear function. It is essentially a modified gradient search in the parameter space. The routine will produce the best-fit value for the coefficients which is a numerical C recipe [Press et al. 1995]. This is accomplished by applying a fitting routine whose input values are rough estimates of the amplitude, A_n, and the rate constant. The routine iterates while monitoring the value of chi squared and continues until convergence is achieved.

4.3.2.1 Displaying ΔR2 Images

Once the ΔR2 images were obtained from the fitting routine they were imported into MATLAB[6], a mathematical and image processing software package. The resultant ΔR2 image is a 256 x 256 matrix that contains information on the dose distribution in the phantom. In MATLAB, image processing and dose conversion can be performed. For this work, a median filter, of size 3 x 3 pixels, was applied to each image to reduce the noise. This filter performs a median filtering of the image in two dimensions. This is accomplished by outputting the median value within a 3 x 3 pixel neighbourhood, an example of which is shown in the Appendix. A typical routine that is used to process the ΔR2 images can also be found in the Appendix. This processing converts the ΔR2 image to a dose image using an equation that will be described in Chapter 5. Once a dose image has been obtained, isodose distributions and depth dose distributions can be created and displayed. Isodose distributions can be obtained using the plotiso(data filename) command in the MATLAB software. Figure 4.4 is an isodose distribution for a 4 cm x 5 cm 9 MeV electron field measured using the MRI gel dosimeter and displayed using MATLAB.

[6] MATLAB - The Math Works Inc.

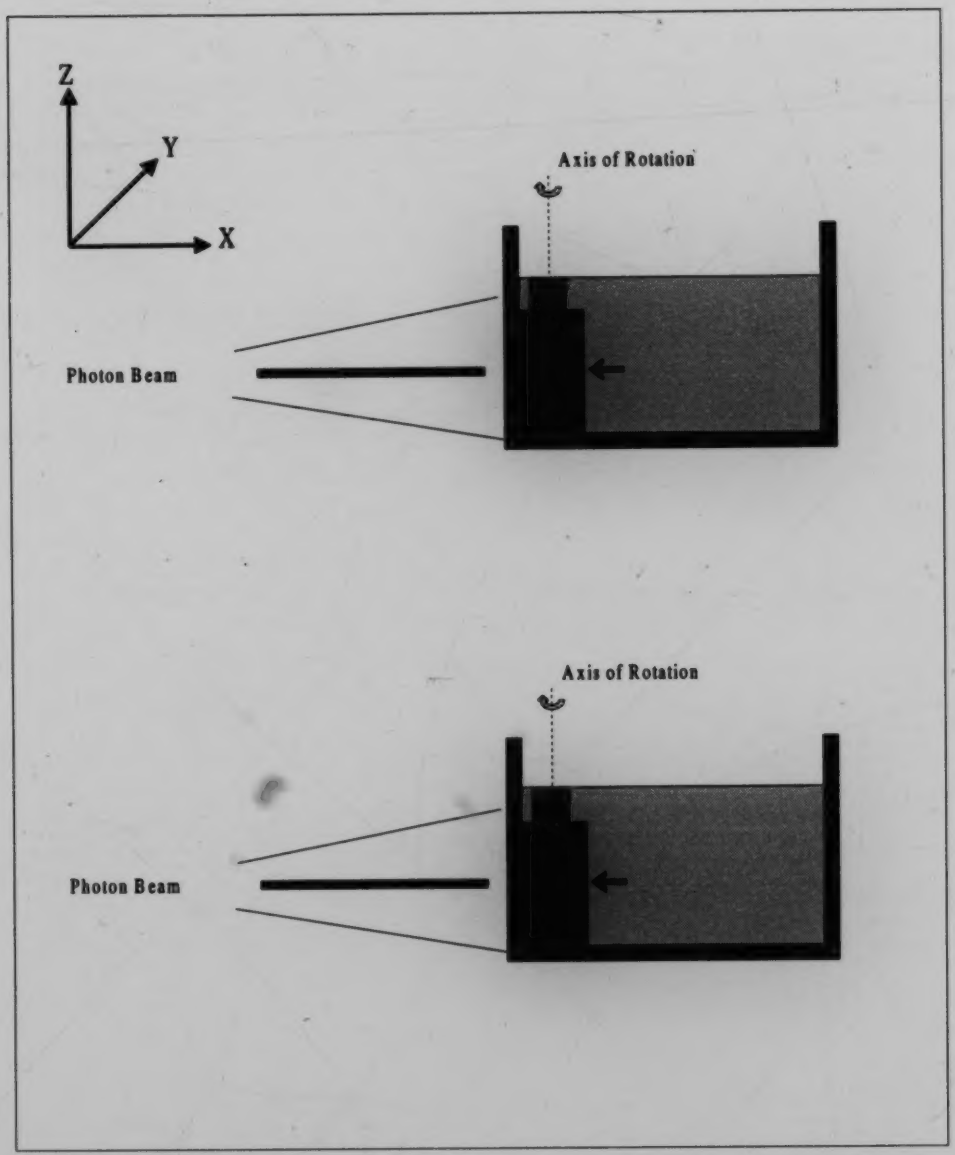

Figure 4.1: A diagram showing the set-up for the photon irradiations to deliver a uniform dose. After the first beam has been delivered, the bottle is rotated 180° degrees and the second beam is then delivered. The arrow indicates the imaging, x-y, plane.

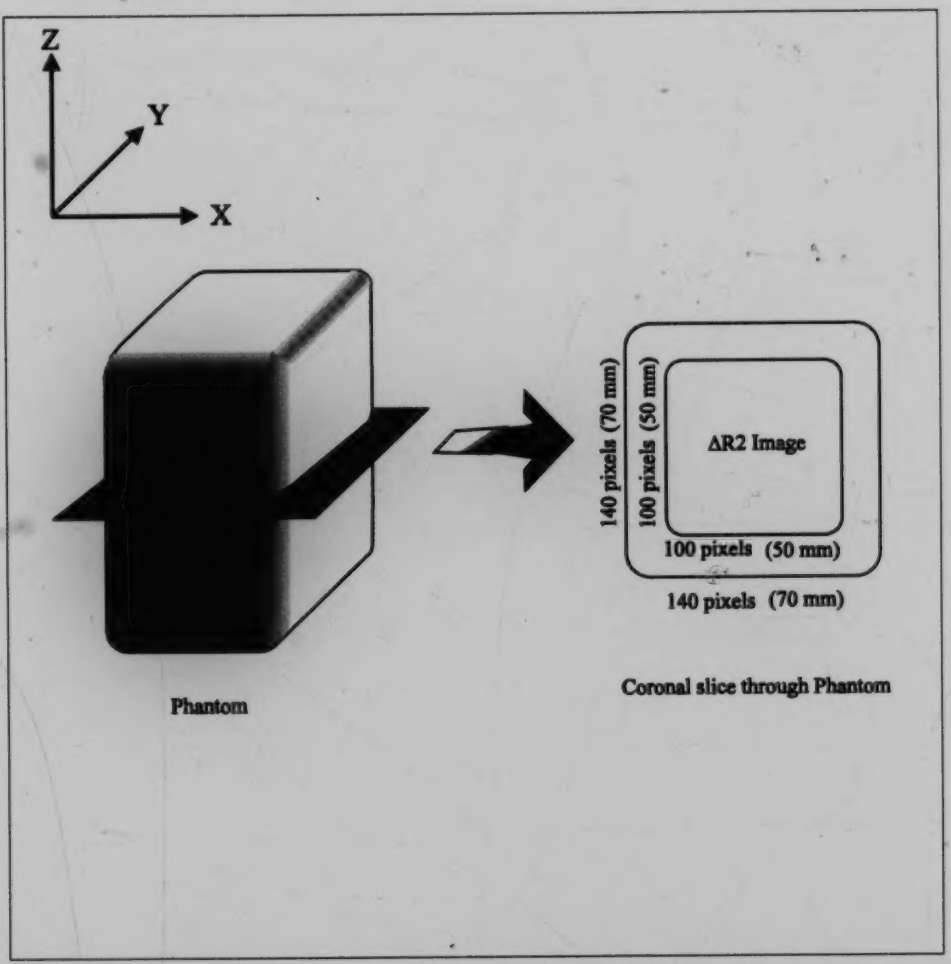

Figure 4.2: A diagram showing the typical plane of interest in the irradiated phantom. The beam enters from the left along the *x*-axis. The distances in brackets assumes that a field of view (FOV) of 128 mm was selected. The orientation in the MR scanner is shown in Figure 4.3.

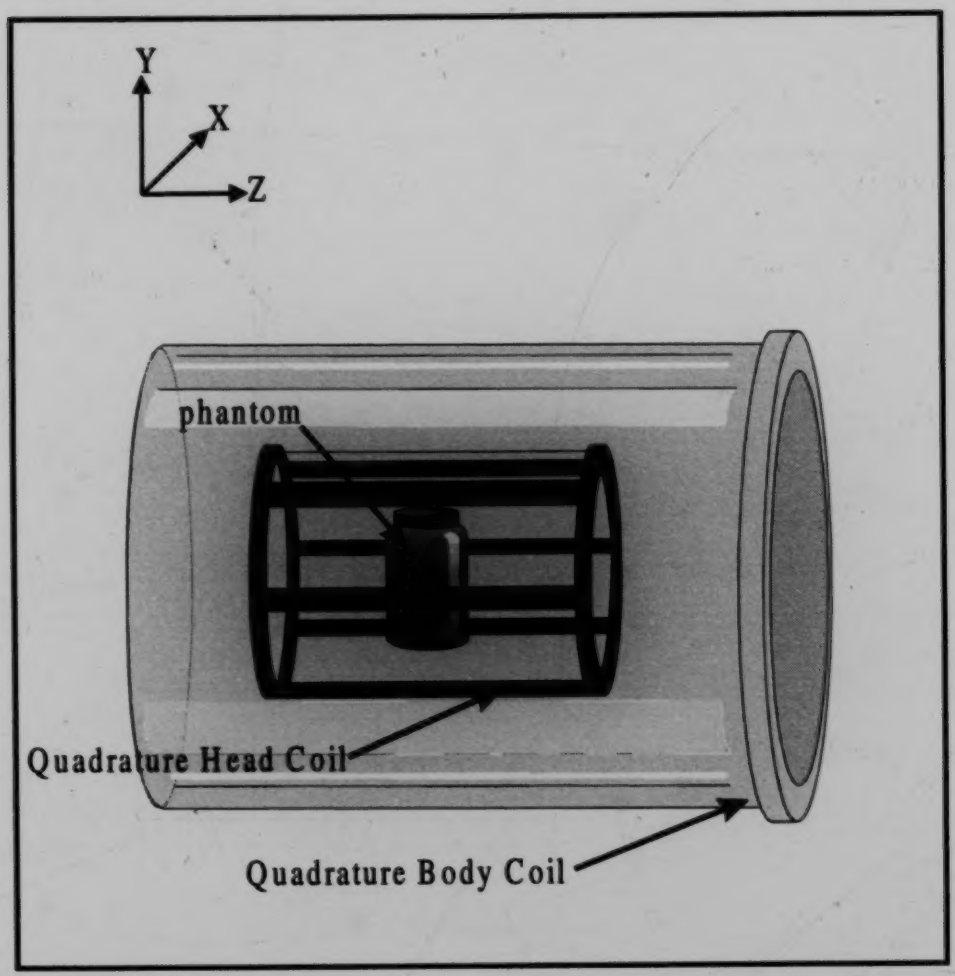

Figure 4.3: A diagram showing the orientation of the phantom within the MRI scanner. The main magnetic field B_0 lies along the *z*-axis. The imaging planes are defined by the co-ordinate axes as follows: *x*-*y* plane = transverse; *x*-z plane = coronal; *y*-z plane = sagittal.

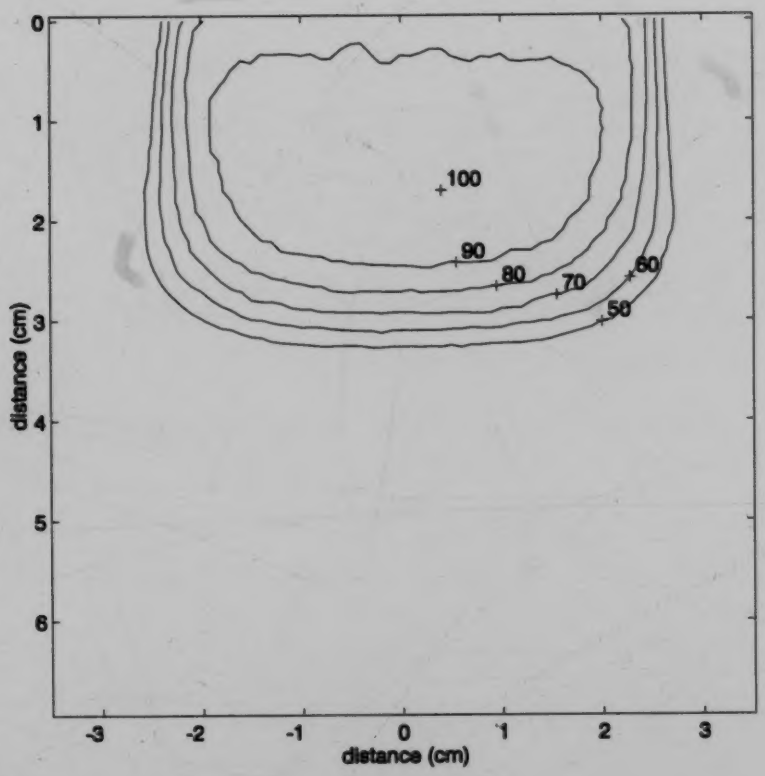

Figure 4.4: An isodose distribution for a 4 cm x 5 cm 9 MeV electron field as displayed in MATLAB. The 100% point corresponds to a dose of 39 Gy.

Chapter 5

Clinical Performance

In this chapter, the results of the dosimeter's clinical performance will be presented. The dosimeter's response to photon beams, electron beams, brachytherapy sources, and certain clinical set-ups involving multiple fields was investigated. In the photon beam studies, the phantoms were irradiated using parallel opposed beams except in the experiment at orthovoltage beam energies of a few hundred keV, and the diffusion experiment. In the electron beam studies, phantoms were irradiated with single beams. For the brachytherapy studies, a high dose rate ^{192}Ir source was used.

5.1 Investigation of the Dose Response due to Photon Beams

A thorough investigation of the Fricke-gelatin dosimeter was performed with respect to its application for photon use. The following properties were examined: uniformity of spatial dose response, dependence on energy, dependence on container used, linearity of dose response, reproducibility and accuracy. Also, the effects of diffusion of the ferric ions was investigated.

5.1.1 Uniformity of Dose Distributions

The square and circular containers referred to in Chapter 4 were filled with Fricke-gelatin of composition 4% gelatin, 1 mM ferrous sulphate and 0.1 M sulphuric acid. They were irradiated uniformly, which reduces dose gradients and the

associated effects of diffusion, to various doses in the range of 5 to 40 Gy. This was accomplished using parallel opposed beams of various energies and the irradiation set-up described in Section 4.2. The expected uniformity along beam axis and across with standard parallel opposed beams, i.e. where the Linac is rotated 180° relative to the phantom after the application of the first beam, is at a level of 1% which is based on measured isodoses. However, with the beam set-up described in Section 4.2, the expected uniformity is at a level of 1 to 2%. This experimental protocol was also used to investigate the dosimeter's dependence on energy, container, and its ability to reproduce dose distributions accurately. The samples were imaged before irradiation and then immediately afterwards.

Before the dependence on either energy or container size could be investigated, it was necessary to determine how uniform the dose would be in the phantom. Figure 4.2 shows the plane of the phantom in which the analysis was done. The beam was delivered along the x-axis and the uniformity was investigated along the same axis. Figure 5.1 shows the data obtained for a typical phantom compared to data obtained through traditional dosimeter techniques, the ion chamber[7] and film[8]. The data obtained from the MRI gel dosimeter was converted to dose from $\Delta R2$ using a predetermined relationship that is described in Section 5.1.3. The ion chamber data were obtained in a water phantom under the same irradiation conditions. The film data were obtained using the same irradiation conditions with the film sandwiched between tissue equivalent blocks of material[9]. The dose measured with the traditional dosimeters appears to be quite uniform across the phantom. The dose measured by the Fricke gelatin dosimeter seems to show a slight increase between -2 and -3.5 cm. However this is comparable with the standard deviation of the data which is 0.8 Gy or 2.7%.

---

[7] IC10 Wellhöfer Dosimetrie
[8] CEA Corporation (Sweden), TVS EP film
[9] Scanplas (U.K.), WTI material.

5.1.2 Dependence on Energy and Shape of Container

Once uniformity of the dose levels within the phantom was established, the dependence of the dosimeter on beam energy was investigated. The dependence of the dose response on beam energy is important for the dosimeter to be effective in the clinical environment, since a wide spectrum of energies is used for the treatment of cancer. Also, the energy of a single photon beam from a Linac varies with respect to the central beam axis. Low energy photons are used for superficial irradiation of skin while high energy photons are used for deep seated tumours. Therefore, a number of square phantoms were irradiated using different beam energies to different dose levels as shown in Figure 5.2. The beam energies investigated were 200 kV, 6 MV, and 15 MV. At 200 kV, the phantom was not irradiated to a uniform dose due to the long irradiation times required, and therefore a single measurement was taken at the surface of the gel. The $\Delta R2$ values, for a 40 Gy exposure, obtained using 200 kV, 6 MV and 15 MV photon beams were 2.24 s^{-1}, 2.22 ± .04 s^{-1} and 2.24 ± .03 s^{-1} respectively. Duzenli [1995] found $\Delta R2$ to be 2.26 s^{-1} for a 40 Gy dose. Thus there is no significant dependence on beam energy within this energy range.

It is important that the dose response of this dosimeter be independent of the size and shape of the container that is utilized. Square and circular phantoms were irradiated uniformly to investigate the possibility of such a dependence. However, data taken at 15 Gy with a beam energy of 15 MV for a circular and a square phantom both yielded $\Delta R2$s of 0.96 ± 0.01 s^{-1}, showing that there seems to be no significant dependence on the shape and size of container used.

5.1.3 Linearity of Dose Response

Because the dose distribution was found earlier to be uniform, 100 by 100 pixel sections, which corresponds to voxel dimensions of 0.5 mm x 0.5 mm x 5 mm,

were isolated from the centre of each image as shown in Figure 4.2. Within this matrix, 10 by 10 sub-sections were isolated and the averages and standard deviations of ΔR2 within each were calculated. This method was used to separate the MRI noise from any non-random, or systematic, variations in the signal. Table 5.1a and 5.1b shows the values of ΔR2 of all sub-matrices within an image obtained from a number of phantoms irradiated to various dose levels with different beam energies, together with the average value of ΔR2 for each dose level.

To investigate the linearity of the dose response, absorbed dose was plotted as a function of the average values of ΔR2 in Figure 5.2. A progressive departure from linearity is evident at high doses and the data were well fitted to a second order polynomial in which the dose, D, is expressed as a function of ΔR2. The equation of best fit, which is plotted in Figure 5.2, was found to be:

$$D = 13.79 \times (\Delta R2) + 1.80 \times (\Delta R2)^2, \qquad (5.1)$$

where D is measured in Grays and ΔR2 in s^{-1}. The dashed line in the Figure indicates the behaviour of the linear term alone.

5.1.4 Reproducibility and Accuracy

A number of square and circular phantoms were irradiated to various doses in the region 5 - 40 Gy. These experiments were repeated 5 to 9 times over a number of months and a few were completed on the same day. A summary of the data can be found in Table 5.1a and 5.1b. For a dose level of 5 Gy, the results obtained were plotted versus time in Figure 5.3. The average value of ΔR2 was calculated to be $0.36 s^{-1}$ and the standard deviation about the mean is 0.02 s^{-1} or 5.6%. The standard deviations about the mean are 0.02, 0.02, 0.03, 0.03, 0.04 for the dose levels of 10, 15, 20, 30 and 40 Gy, respectively. This corresponds to a level of reproducibility that

ranges from 5.6% at a low dose level to 2% at a radiation dose of 40 Gy. These standard deviations are roughly independent of the dose level and the main reason for the differences is random error associated with noise from the MRI scanner. At low dose there is less signal than at high dose due to the smaller number of ferric ions present, so at low doses there is a higher signal to noise ratio. There are many factors that affect the reproducibility of the dosimeter, two of which will be discussed further. There is an uncertainty associated with the irradiation geometry, which introduces an error of 1% for a 5 mm mis-alignment. Also, due mainly to uncertainties in attaining precise concentrations, there is an error of approximately 1% associated with the composition of the phantom.

The accuracy of the dosimeter is a measure of how the measured data conforms to the expected or theoretical dose. To determine how accurate this dosimeter was, it was compared to the measurements obtained with a standard ion chamber[10]. The results of an experiment conducted at 200 kV are plotted in Figure 5.4 and compared with data obtained with the ion chamber. The general shapes of the curves agree with each other but it is apparent that there is a systematic discrepancy. This was determined to be approximately 3% and the data set was therefore scaled by a factor of 1.03. It is believed that the systematic discrepancy stems from variations in the output of the machine varies in the orthovoltage energy range and the fact that the data obtained from the ion chamber is only measured at a few points, the line being an interpolation between these measured points. The standard deviation of the scaled data relative to the standard ion chamber data was 3%.

A reduction in accuracy was detected at the walls of the container. This effect is seen as a ringing at each end of a dose profile as seen in Figure 5.5. This will pose a problem in a clinical case if accurate readout of the images is required within 5 mm of the surface of the container. There are many possible reasons for this "wall effect" which include: the echo quotient analysis if the phantoms were not in the same

[10] IC10 Wellhöfer Dosimetrie

position before and after irradiation; and within each echo there is slight physical movement of the phantom due to vibrations caused by the gradients switching on and off. However, these problems are likely to be unimportant in practice except for the vibrations in the gel due to the switching of the gradients[11].

5.1.5 Diffusion effects

Due to the fact that the ferric ions tend to diffuse after irradiation, the time between irradiation and post-irradiation imaging may be important. Ideally, post-irradiation imaging should be accomplished immediately after irradiation but Shultz *et al.* (1990) found that a delay of up to an hour would result in minimal degradation of the spatial information. This result was checked by filling a square container with the Fricke-gelatin which was irradiated to 20 Gy at d_{max} with a 4 cm x 4 cm 15 MV photon beam. The post irradiation images were acquired with time delays between irradiation and imaging of 10 minutes, then 2, 4, and 6 hours. Figure 5.6 depicts the type of degradation of the spatial information that occurs due to diffusion of the ions. Figure 5.7 depicts the widening of the penumbra width with time obtained from Figure 5.6 and a number of other phantoms irradiated the same way. The penumbra width is taken to be the difference between the width at the 80% and 20% dose levels. The measured penumbra of beams obtained with diode dosimeters was found to be 5 mm. This data set shows that imaging should be performed within 1 hour after irradiation to ensure that the blurring of the images caused by diffusion will be less than 1mm.

[11] Duzenli 1996 - private communication

5.2 Investigation of the Dose Response for Electron Beams

The purpose of this experiment was to investigate the possibility of an over-response of dose, i.e. the dose is greater than expected at the beam entrance at the surface of the gel, when using electron beams. Previous studies had indicated that there was a surface over-response for electrons [Olsson 1990, Duzenli 1995]. In Olsson's experiment, the beam was directed through a 1 mm thick entrance window made of Perspex, while in Duzenli's experiment, the surface of the gel was exposed to the atmosphere during irradiation.

For this experiment, square and rectangular containers containing Fricke-gelatin were irradiated to a dose level of 40 Gy using 9 MeV beams. Three different set-ups were used: irradiation through the side of the container (thickness = 1.52 mm); irradiation through the surface when it was exposed; and irradiation through thin food wrap (thickness = 0.02 mm) covering the surface of the gel. The central axis depth doses for each set-up are plotted in Figure 5.8. The depth dose distribution in the phantom where the surface was exposed to the atmosphere during irradiation shows an over-response which is most likely due to the diffusion of oxygen from the atmosphere into the gel. Duzenli [1995] observed an oxygenation effect, which manifested itself as an increase in the dose response, when she varied the amount of gel in small column tubes which were about 30 mm in length. The response is significantly reduced when the phantom was covered by the thin food wrap during irradiation. For best results, radiation should therefore not be imparted on the exposed surface of the gel. The shape of the depth dose for the gel irradiated through the side of the container is the same as that of the gel irradiated through the food wrap which covered the surface of the gel, but there is a difference in the maximum dose registered in each case. This was investigated further in the second part of this section, along with the dependence of the dose response on electron beam energy.

For the following experiment, a number of square phantoms were irradiated through the side of the phantom container with electron beams with energies of 9, 12, and 18 MeV. The depth dose curves obtained from the MRI dosimeter for each energy, along with the corresponding ion chamber data, was plotted in Figure 5.9. Ion chamber data were not available for a 12 MeV electron beam with a field size of 4 x 5 cm^2, therefore the MRI data is compared with ion chamber data obtained with a 4 x 4 cm^2 field. For the 12 MeV MRI measured data set, there is a small discrepancy at depth which could be accounted for by the difference in the field sizes or by a shift in the determination of the surface of the gel. The shapes of all the curves agree well with the ion chamber data. However, there seems to be a systematic error in the dose calibration that was used. The 9 MeV and 18 MeV depth dose curves, which were obtained on the same day, show a reduced dose registered at d_{max} whereas the 12 MeV depth dose curve, obtained on a different occasion, shows an increased dose at d_{max}. This indicates that the precision that can be obtained for absolute dosimetry for electrons is only about 5%. However the absolute accuracy of the dosimetry for electrons is not expected to be better than 2%. The conversion relationship that was used for this electron study was that obtained from the photon irradiation experiments, suggesting that a conversion relationship for electrons may need to be determined independently. The depth dose data does not demonstrate a correlation with beam energy and the discrepancy in dose, although it does seem to indicate that the electron dosimetry is more sensitive to phantom and irradiation conditions than that found with photons.

5.3 Investigations of the Dose Response for an Ir-192 Brachytherapy Source

For these brachytherapy irradiation experiments, the circular containers, which were described in Chapter 4, were filled with Fricke-gelatin along with plastic catheters, to house the source. Two different experiments were performed to investigate the dosimeter's response. A single catheter was used for both single dwell time and multiple dwell time experiments. Dwell time is the amount of time the source remains in a designated position in the catheter. Therefore in a single dwell time experiment the source remains in one position for the entire irradiation time whereas for the multiple dwell time experiment, the source is moved to different positions in the catheter after remaining in a particular position for the specified time, in order to generate dose distributions of a desired shape.

For the single dwell time experiment, a dose of 20 Gy was delivered to a point 2 cm away from the axis of the source. Figure 5.10 shows a radial profile of the dose distribution. The fact that the dose tends to "roll over" in the middle is due to the high dose values near the catheter; the dose response for this dosimeter using $\Delta R2$ as a measure is known to "roll over" around 100 Gy [Duzenli 1995]. Apart from that, the dose distribution agreed well with what was expected on the basis of the inverse square law. At a point 2 cm away from the central axis, a $\Delta R2$ value of $1.30 \pm 0.03\ s^{-1}$ was obtained. This value is about 4% higher than that found in the photon studies previously discussed for a dose of 20 Gy. Considering the high dose gradients, this is excellent agreement.

For the multi-dwell time experiment, a dose of 10 Gy was delivered to the reference depth, which is approximately 1.5 cm away from the central axis. The dwell times were computed[12] to give a uniform dose at a distance of 1.5 cm away from the axis of the catheter. The $\Delta R2$ obtained from this point was $0.61 \pm 0.03\ s^{-1}$ which is about 7% less than what was found with the photon irradiations.

Determining the position of these depths is less accurate than in an external beam irradiation. Due to the after-loading technique for delivery of the brachytherapy source, described in section 4.2, there is more of a chance of movement of the catheter during irradiation, especially during the loading and unloading of the source, which reduces the accuracy in determining the location of the edge of the catheter, and thus in determining the reference depth at which the dose was delivered.

5.4 Clinical Applications

As a test to see how this dosimeter would perform in the clinical environment, two clinical studies were done. The first was an investigation of the dose near the junction of a photon beam and an electron beam in a head and neck case study. The second involved a two catheter brachytherapy irradiation set up.

5.4.1 Head and Neck Study

For some patients with head and neck cancers, protocols call for the radiation dose to be delivered using both a photon and an electron beam, the electron beam being used to irradiate the nodal region in the neck because of its depth dose characteristics. If the beams are placed adjacent to one another, the electrons will scatter and cause an excessive dose, a "hot spot", in the nearby region which is irradiated by the photon beam. It is important to ensure that this hot spot does not occur near a critical structure such as the spinal cord. A study was therefore conducted to search for the "hot spot" that might arise near the junction of the photon beam and electron beam. In this study, a 10 cm x 10 cm 6 MV anterior photon beam was used with a lateral 10 cm x 10 cm 9 MeV electron beam as shown in Figure 5.11. A cylindrical container, whose diameter is 15.2 cm and height is 20.6 cm, was filled

[12] Nucletron Planning system BPS software v. 11.4

with Fricke-gelatin and irradiated by the two beams, first by the electron beam followed by the photon beam. The cylindrical phantom was used as a representation of the head and neck anatomical geometry. A dose of 40 Gy was delivered to d_{max} for both beams. The two beams were placed orthogonal to one another and the central axis of the beams were aimed 45° from the vertical axis on the surface of the cylinder. The divergence of the beams did not pose much of a problem, as there was not much curvature due to the cylinder, when the edge of each beam was matched at the phantom surface. Figure 5.11 shows the location of the planes that were imaged to investigate the junction of the two beams. The results showed that there is a hot spot, 25% above the baseline dose, in the photon region, while a cold spot, 10% below the baseline dose, is observed in the electron region as shown in Figure 5.12. To verify using another dosimeter, that these results are what would be expected would be difficult to do, due to the geometry that was used, i.e. the curved surface of the phantom. This is the problem that arises in many clinical cases and indicates why the MRI gel dosimeter is needed to provide a tool for treatment verification. However, an isodose distribution was obtained from a plan performed on the Helax[13] three-dimensional treatment planning system, and compared with that obtained from the MRI dosimeter, as shown in Figure 5.13. There is good qualitative agreement between the two, with the shapes of the isodose curves being very similar.

5.4.1 Two Catheter Brachytherapy Study

For patients with certain cancers that are small in volume, brachytherapy treatment is sometimes prescribed. The normal course of treatment is to place a number of catheters so as to ensure that there is a uniform dose distribution that encompasses the tumour. The brachytherapy source used was the microSelectron HDR ^{192}Ir source , which was loaded into two catheters set in Fricke gelatin. The

[13] Helax TMS, Sweden

catheters were arranged to mimic an intra-luminal bronchus treatment at the carina, which is the branching point of the mainstem bronchus. Irradiation was done consecutively in both catheters. The dose was prescribed to deliver 15 Gy at a distance of 1 cm away from the catheters. The dwell times were calculated[14] to give 15 Gy at a distance of 1 cm from the axis of the catheter. The $\Delta R2$ values were converted to dose using the dose conversion equation determined in Section 5.1.3. The results obtained from this experiment are displayed in Figure 5.14. The shapes of the isodose curves are what is expected from treatment planning calculations, which are not shown. Therefore, this dosimeter can handle brachytherapy irradiation set-ups of a clinical nature.

[14] Nucletron Planning system, BPS v. 11.4 software

Table 5.1a: ΔR2 data, measured in s^{-1}, from various phantoms irradiated with different beam energies, 6 MV and 15 MV, to uniform dose levels of 5, 10 and 15 Gy.

Beam Energy	Phantom #	5 Gy	10 Gy	15 Gy
6	1	0.36 ± 0.03	0.65 ± 0.02	0.93 ± 0.04
6	2	0.33 ± 0.03	0.64 ± 0.06	0.98 ± 0.03
6	3	0.35 ± 0.02	0.65 ± 0.03	0.93 ± 0.04
15	4	0.39 ± 0.03	0.60 ± 0.02	0.96 ± 0.01
15	5	0.37 ± 0.01	0.66 ± 0.04	0.96 ± 0.01
15	6	0.35 ± 0.02	0.61 ± 0.02	0.96 ± 0.03
6	7	0.37± 0.01	0.64 ± 0.01	
15	8	0.34 ± 0.02		
15	9	0.38 ± 0.02		
Avg.		0.36 ± 0.02	0.64 ± 0.02	0.95 ± 0.02
Fit		0.34	0.66	0.96

Table 5.1b: ΔR2 data, measured in s^{-1}, from various phantoms irradiated with different beam energies, 6 MV and 15 MV, to uniform dose levels of 20, 30 and 40 Gy.

Beam Energy	Phantom #	20 Gy	30 Gy	40 Gy
6	1	1.28 ± 0.01	1.84 ± 0.03	2.21 ± 0.03
6	2	1.26 ± 0.02	1.78 ± 0.03	2.22 ± 0.04
6	3	1.24 ± 0.03	1.76 ± 0.07	2.19 ± 0.04
15	4	1.30 ± 0.08	1.80 ± 0.05	2.31 ± 0.09
15	5	1.24 ± 0.01	1.76 ± 0.01	2.24 ± 0.03
15	6			
6	7			
15	8			
15	9			
Avg.		1.26 ± 0.03	1.79 ± 0.03	2.23 ± 0.04
Fit		1.25	1.78	2.24

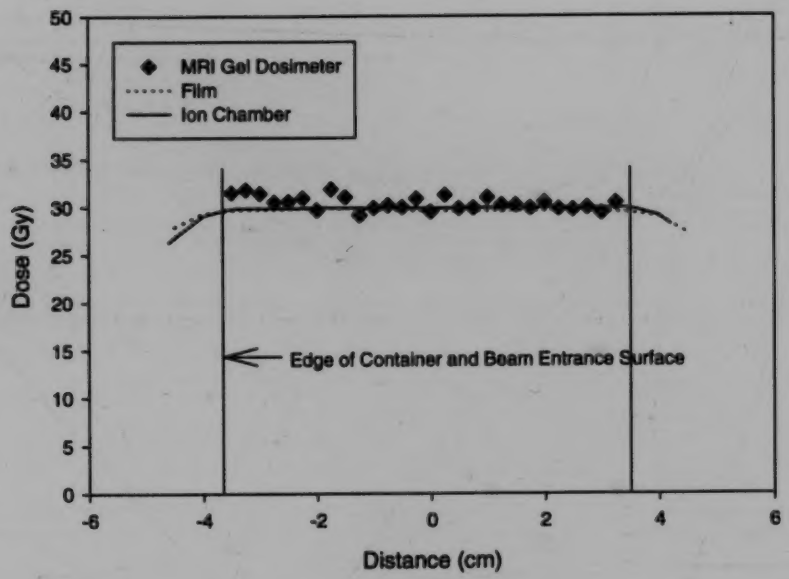

Figure 5.1: Variation of the dose along the axis of the beam for a phantom irradiated to 30 Gy. Also shown are data obtained with traditional dosimeters.

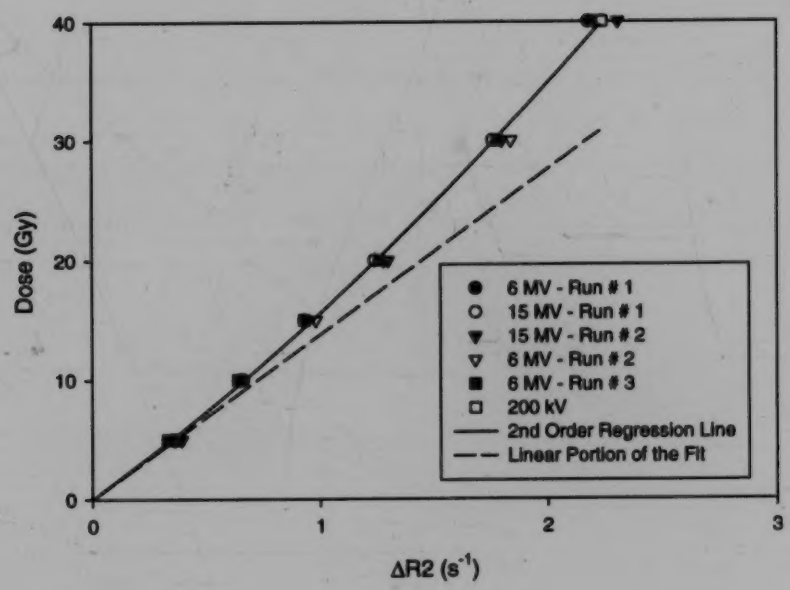

Figure 5.2: Absorbed dose plotted versus ΔR2 at various photon energies. The curve is a plot of Equation 5.1. The dashed line indicates the behaviour of the linear term alone.

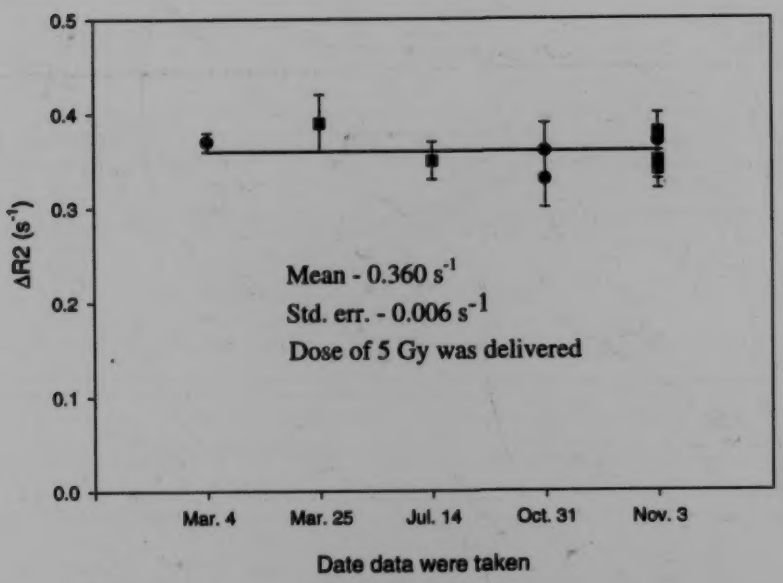

Figure 5.3: Data representing short term and long term reproducibility for phantoms irradiated uniformly using parallel opposed beams to a dose of 5 Gy. The beam energies used were 6 MV, indicated by the solid circles, and 15 MV, indicated by the solid squares. The phantom readout was that described in section 5.1.3. The horizontal line shows the mean value of 0.36 s^{-1}. The standard deviation about the mean is 0.02 s^{-1}.

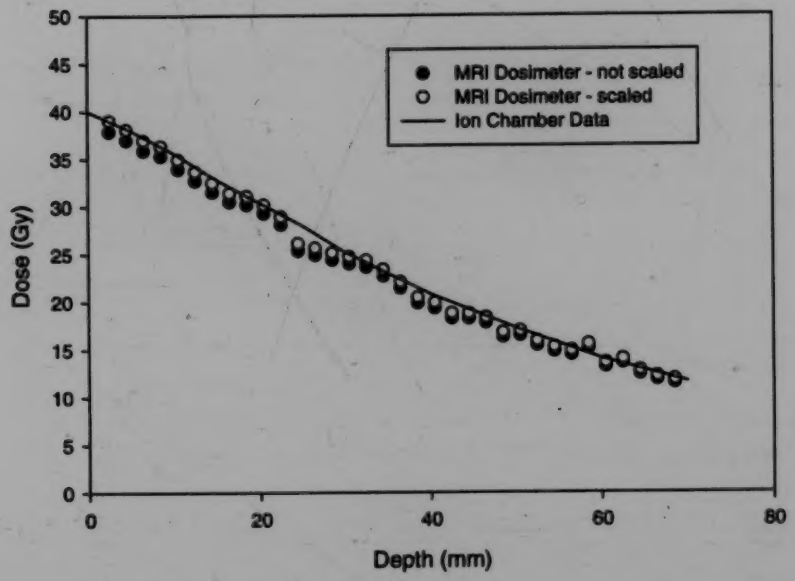

Figure 5.4: Depth dose curve for 200 kV photons at a dose of 40 Gy. This was a single beam irradiation technique. The solid circles are the data obtained using the MRI gel dosimeter and the open circles are the scaled MRI gel dosimeter data. The data obtained with an ion chamber is indicated by the solid line.

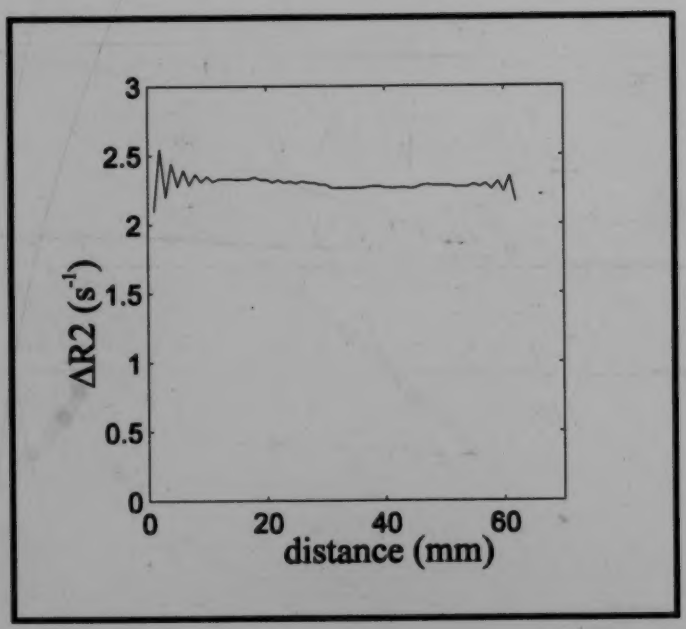

Figure 5.5: ΔR2 profile taken on the axis along which the beam was delivered. This profile illustrates a ringing at the edge of the square phantom when it was irradiated to 40 Gy with a photon beam of energy 6 MV.

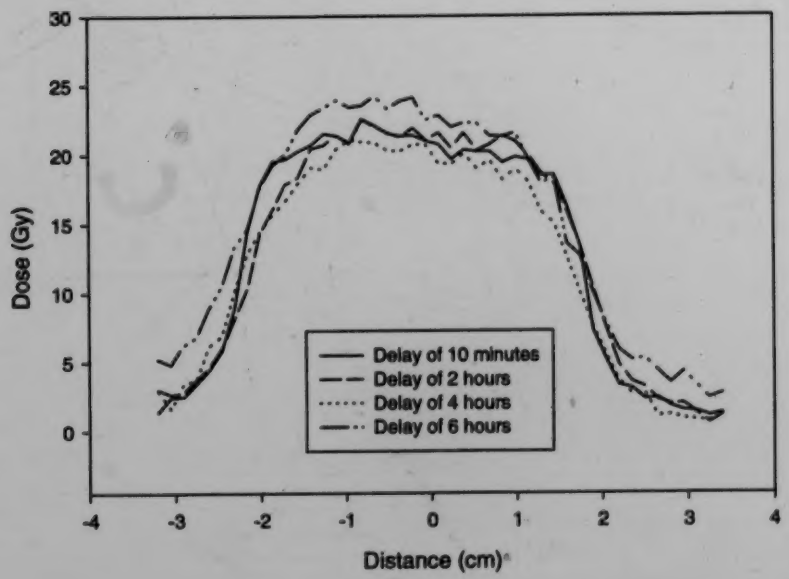

Figure 5.6: Dose Profiles at a depth of 2 cm across the beam axis of a 4 cm x 4 cm, 15 MV photon field measured at various post irradiation times.

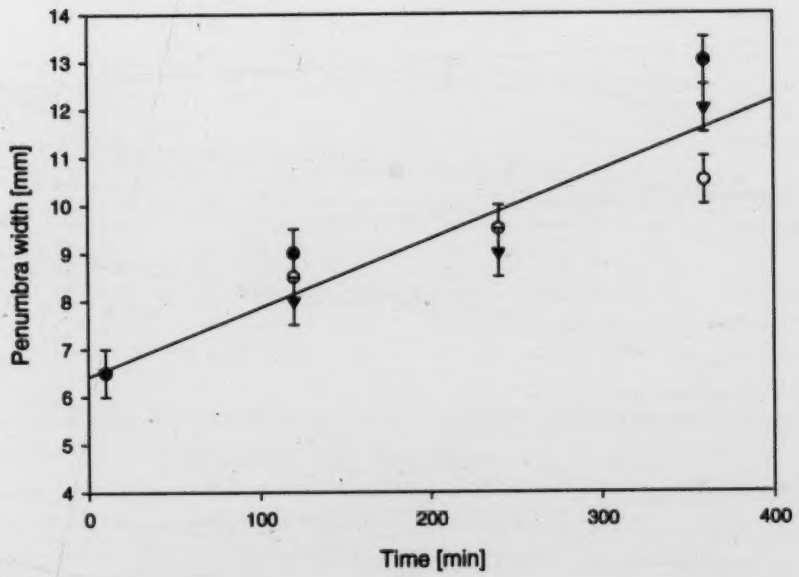

Figure 5.7: The width of the penumbra of a 15 MV photon beam plotted as a function of time after irradiation in a number of dosimeter gels. The open and closed circles and solid triangles refer to three phantoms, all prepared in the same manner, irradiated with a single photon beam. The penumbra width was taken to be the distance between the 80% and 20% dose levels of profiles such as that in Figure 5.6.

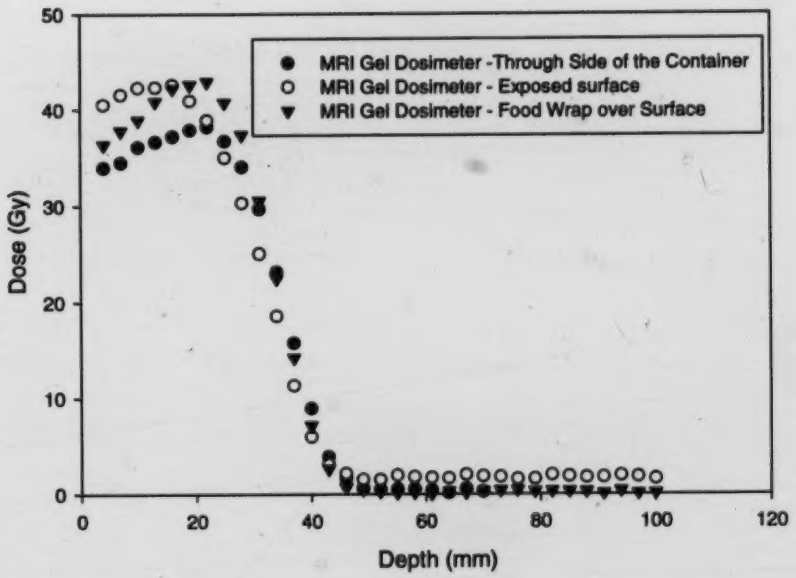

Figure 5.8: A comparison of the depth dose profiles for 9 MeV electron beams along the beam axis when the phantoms were irradiated to 40 Gy with the beam directed through the side of the container, onto the exposed surface of the Fricke gel, and through food wrap placed over the surface.

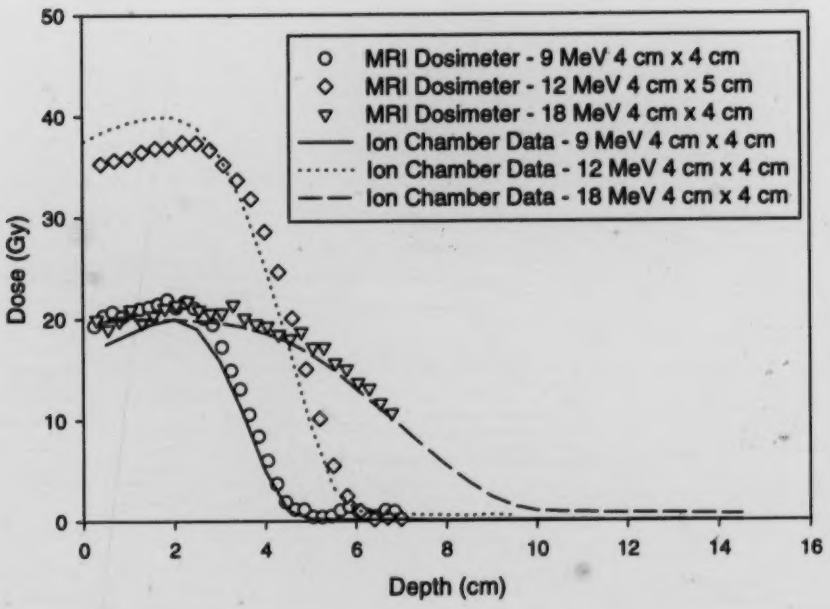

Figure 5.9: A comparison of the depth doses for 9, 12 and 18 MeV electron beams along the beam axis. The phantoms were irradiated to either 20 or 40 Gy.

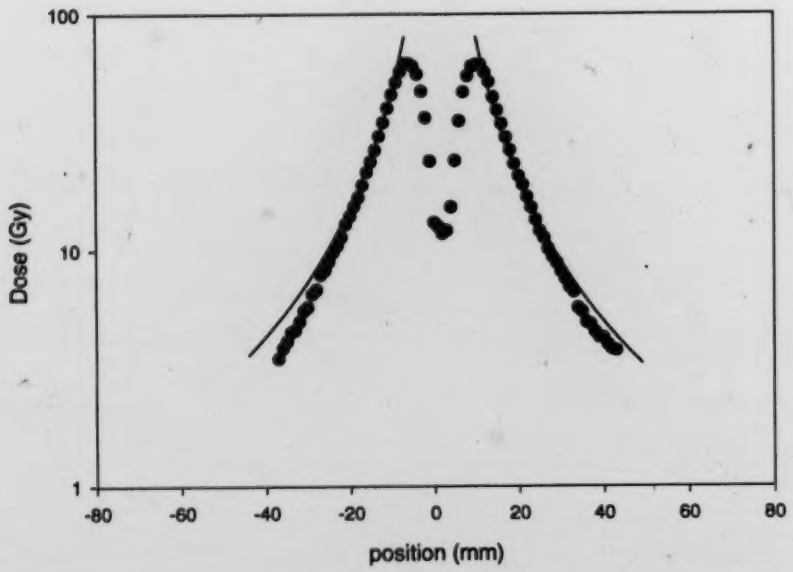

Figure 5.10: Dose profile along the perpendicular bisector of a MicroSelectron ^{192}Ir source. The closed circles indicate the dose obtained using the MRI dosimeter, while the curve indicates the dose which is expected, assuming an inverse square law dependence.

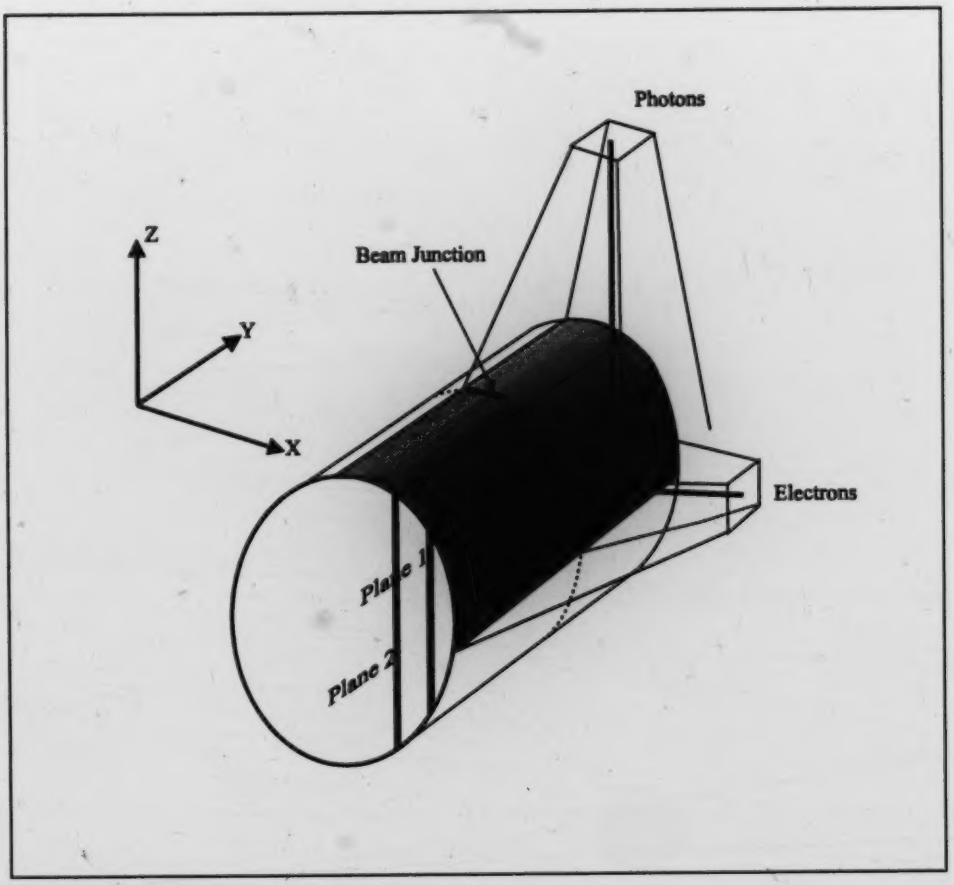

Figure 5.11: Diagram depicting the irradiation set-up for the head and neck case study. The slices investigated were planes 1 and 2.

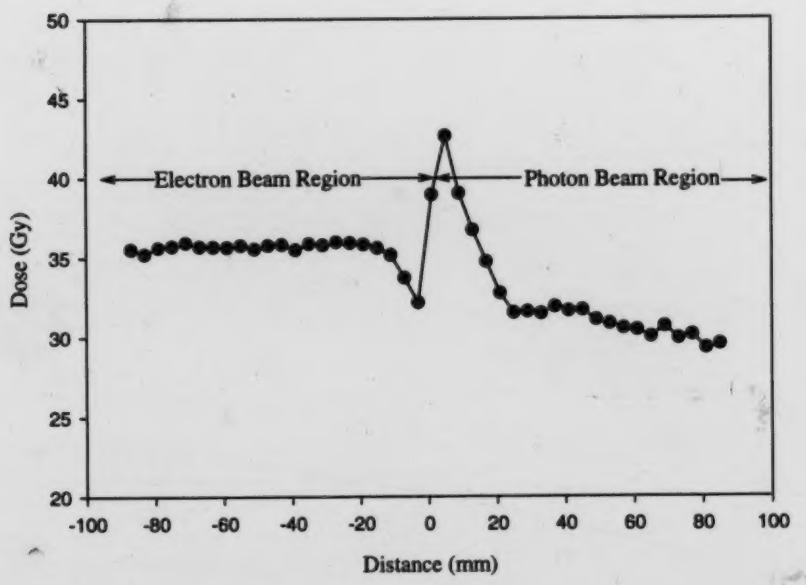

Figure 5.12: Dose profile generated by delivery of an electron beam alongside a photon beam in the head and neck clinical case study. The profile is along the y - axis, taken from plane 1 at a depth of 10 mm. The electron beam was delivered to the left half while the photon beam was delivered to the right half. This profile indicates that there is a hot spot in the photon region and a cold spot in the electron region due to the lateral scattering of the electrons.

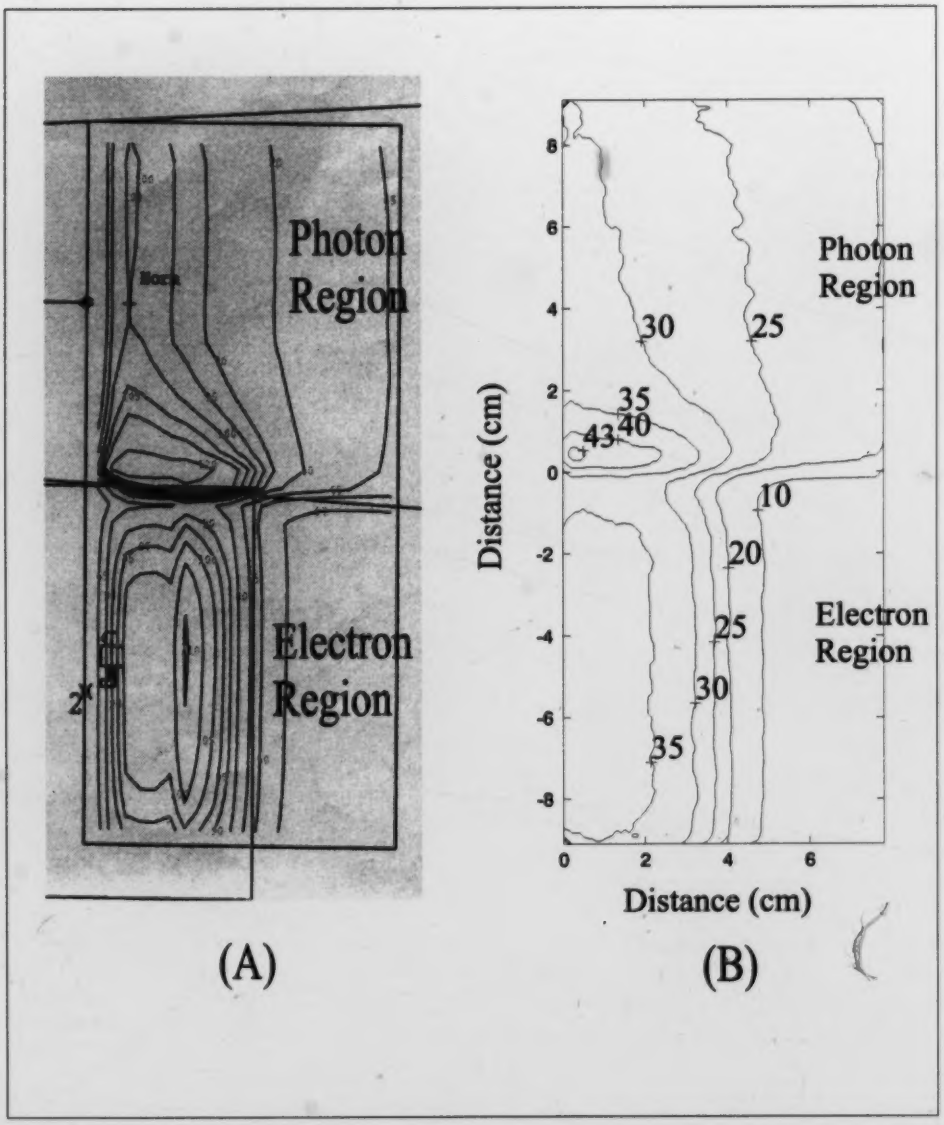

Figure 5.13: A comparison of isodose distributions obtained from a) Helax treatment planning system and b) MRI gel dosimeter for the head and neck irradiation set-up. This isodose distribution is taken from plane 1 as defined in Figure 5.11. The hot spot is located at the position of 43 Gy which is 25 % above the base line dose, 35 Gy, in the photon region.

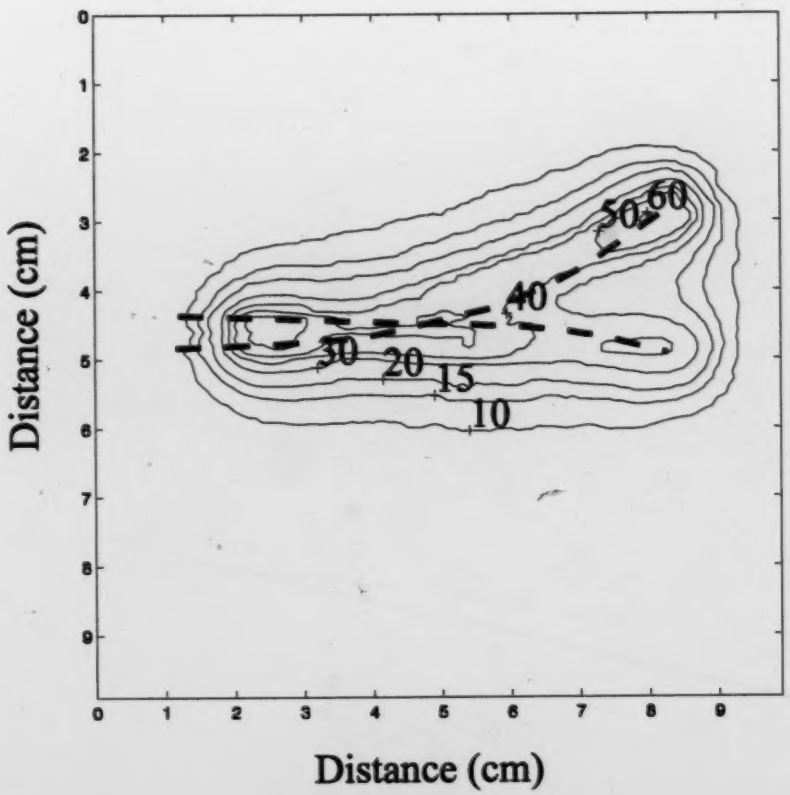

Figure 5.14: Dose distribution for a two catheter brachytherapy irradiation. This is an simulation of a two catheter bronchus irradiation. The location of the catheters is indicated by the dashed lines. At the crossover point, the separation of the two catheters was about 5 mm.

Chapter 6

Investigation of Relaxivity of Ferric and Ferrous Ions

As discussed in Section 3.4, relaxivity is used to measure the dose response of the dosimeter. If the relaxivity of the ferric ion can be increased, while that of the ferrous ion remains constant, then the sensitivity of the dosimeter would increase, because the dose measurement is dependent upon the difference in the relaxivities of the two ions. The relaxivity of the ferric ion has been found to increase with increasing field strength of the MRI scanner [Duzenli *et al.*, 1994]. If this is true, then when clinical scanners are upgraded to higher field strengths, this dosimeter would be more sensitive for determining dose distributions. Presently at the Cross Cancer Institute, the clinical scanner[15] available is a 1.5 T magnet, but there was available a 3 T research magnet[16] in which studies on the relaxivity of the ions were conducted. This chapter will focus on the results that were obtained for the relaxivity of the ferric and ferrous ions at both field strengths.

6.1 Materials and Methods

Ferric and ferrous sulphate solutions were prepared using analytical reagent grade ferric sulphate, $Fe_2(SO_4)_3$, ferrous sulphate, $FeSO_4$, sulphuric acid, H_2SO_4, and distilled deionized water. A dilution technique was used to obtain the lower concentrations starting with approximately 1 mM ferric or ferrous ion solutions. The

---

[15] Philips Gyroscan
[16] University of Alberta In-vivo Research Magnet

concentration of the sulphuric acid was held constant at 0.15 M to ensure that the pH remained around 1. Such low pH ensures rapid proton exchange and increases the solubility of the ions [Koenig and Brown 1984]. Measurements were made at both 1.5 Tesla and 3 Tesla. At 1.5 Tesla, the solutions were placed in 30 ml containers and imaged. The imaging sequence used was a phase-alternated CPMG sequence with 8 echoes, TE = 50 ms, TR = 2000 ms, and number of excitations NEX = 2. At 3 Tesla, the solutions were placed in the same 30 ml containers and T2 values were obtained using a CPMG sequence with phase cycling and TE = 1.6 ms, TR = 20 s, NEX = 4, and $B_1 = 6 \times 10^{-4}$ T, where B_1 is the magnitude of the rf field.

6.2 Results and Discussion

The relaxation rate R2 is plotted against the concentrations of the ions Fe^{3+} and Fe^{2+} in Figures 6.1 and 6.2, respectively. These plots were found to be linear in the region of interest. The ferrous ion is not a very strong paramagnetic ion, therefore the relaxation times at very low concentrations are very similar to pure water and so are harder to measure accurately using imaging techniques.

The relaxivities of the ferric and ferrous ions were determined from the slopes of the graphs of R2 versus ion concentration. The relaxivity of the ferrous ion was found to be 1.17 ± 0.06 $s^{-1}mM^{-1}$ and 1.01 ± 0.07 $s^{-1}mM^{-1}$ at 1.5 T and 3 T respectively. The relaxivity of the ferric ion was found to be 11.7 ± 0.6 $s^{-1}mM^{-1}$ and 16.9 ± 0.6 $s^{-1}mM^{-1}$ at 1.5 T and 3 T respectively. Therefore, the relaxivity at 3 Tesla was found to be 44% higher than that at 1.5 Tesla for the ferric ion. For ferrous ions, the relaxivity of showed no significant difference although the two values are not within error, the relaxivity at 1.5 T was obtained from a fit of only 3 points, therefore the error in the measurement should be higher.

These values are plotted against proton resonance frequency in Figure 6.3 along with a compilation of values found in the literature. Also plotted in Figure 6.3

are the theoretical predictions of the relaxivity due to dipolar and hyperfine interactions which were determined from Equations 3.21 and 3.24 found in Chapter 3. It can be seen that the experimental values are in good agreement with theory. Previously it had been postulated that the term that dominated the relaxation process of the protons in the presence of ferric ion was the dipole-dipole term, and that the contact term had little or no role in this process [Gore *et al.* 1984]. However, it can be seen that the contact interaction in the case of the ferric ion is important at higher frequencies.

The sensitivity of the dosimeter depends upon the relaxivities of the ferric and ferrous ions. Since the relaxivity of the ferric ion increased by going to higher field strength, the Fricke gel dosimeter has the potential to perform better due to an increase in sensitivity. This study was conducted with liquid ferric ions, however previous studies have indicated that the relaxivity in the gel system should behave in the same manner [Duzenli 1995].

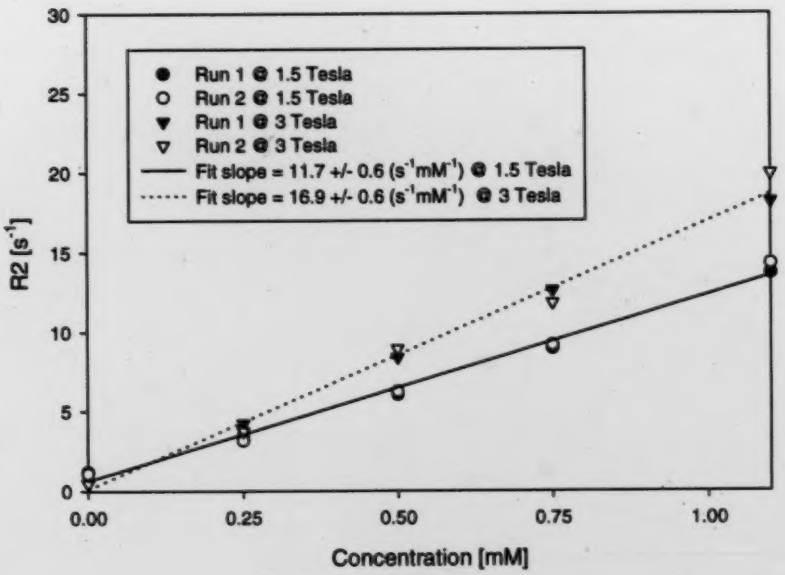

Figure 6.1: R2 vs. Fe^{3+} ion concentrations for aqueous solutions at 1.5 Tesla and 3 Tesla.

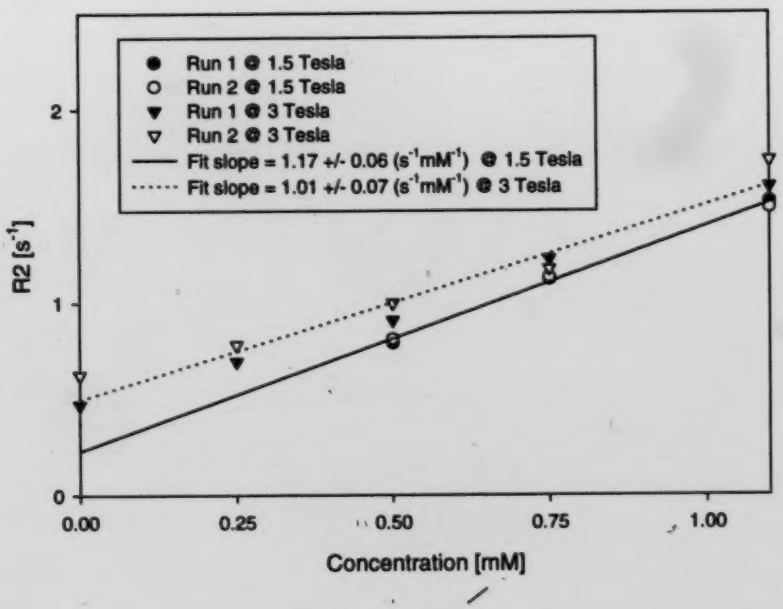

Figure 6.2: R2 vs. Fe^{2+} ion concentrations for aqueous solutions at 1.5 Tesla and 3 Tesla.

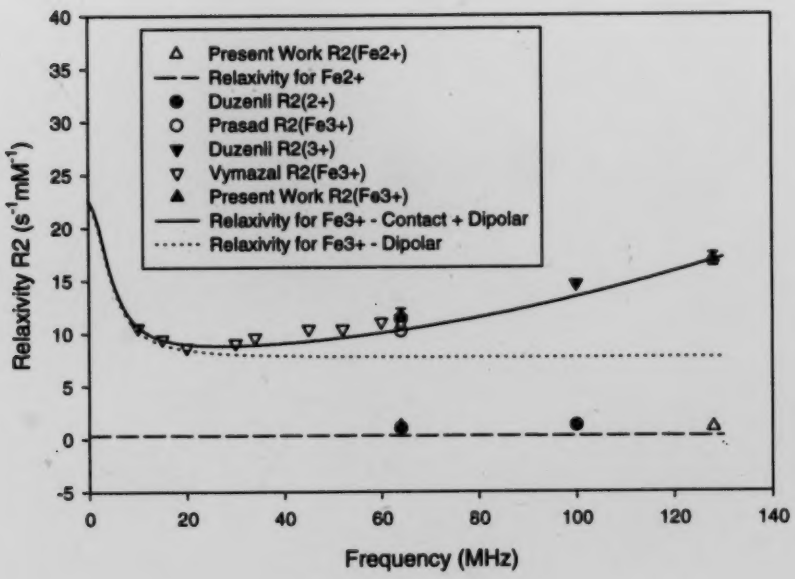

Figure 6.3: Relaxivity R2 of ferric and ferrous ions versus proton resonance frequency. The symbols represent measured data from various authors. The line and the curves indicate theoretical predictions.

Chapter 7

Summary and Conclusions

The potential of the MRI gel dosimeter as a clinical dosimeter has been investigated by observing its clinical performance and performing a number of reference tests.

The Fricke-gel composition used in this work was 0.05 M sulphuric acid, 4% gelatin by weight and 1 mM ferrous sulphate. The dose response of the dosimeter to the application of external beams and brachytherapy was investigated. Instead of using R2 as a measure of dose, ΔR2 was used. ΔR2 is the parameter which provides information on the chemical change and is measured by taking the ratio of the post-irradiation to pre-irradiation images as proposed by Duzenli et. al. [1995]. This analysis of the dose response using ΔR2 as a measure reduces the amount of error due to stimulated echoes produced in clinical MRI scanners.

For the photon studies, it was shown that there is no significant dependence on beam energy and no significant dependence on the shape and size of container used. The calibration equation that converts ΔR2 to dose was found to be non-linear in the range of 5 - 40 Gy. The equation of best fit was found to be:

$$D = 13.79 \times (\Delta R2) + 1.80 \times (\Delta R2)^2,$$

where dose, D, is measured in Grays and ΔR2 in s^{-1}. The reproducibility of the dose response of the dosimeter was found to be achievable at a level of 5 - 6% at low dose, i.e. 5 Gy, but improves to a level of 2% at higher doses, i.e. 30 - 40 Gy. The accuracy

of the absolute dose response as compared with other dosimeters was found to be within 10%, although the accuracy of the relative dose response is much better and is within 5%. Due to the diffusion of the ferric ions, the data show that images should be taken within 1 hour after irradiation to ensure that the blurring of the images will be less than 1 mm.

For the electron beam studies, it was found that to achieve the best results, radiation should not be imparted on the exposed surface of the gel but should be imparted through the side of the phantom because of the over-response of dose that is seen at the surface of gels. The electron depth dose curves measured with this dosimeter agree well with data obtained with ion chambers but the accuracy of the absolute dosimetry has to be investigated more thoroughly. This dosimeter will perform excellently as a relative dosimeter with respect to electron beam therapy.

The absolute dosimetry of this dosimeter was found to be accurate to within 10% which is not acceptable by the International Commission on Radiation Units and Measurements (ICRU) standards [ICRU 24 1976]. To account for this large discrepancy would require investigations looking for a systematic error which would be the major component of the error. Presently, errors in both irradiation set-up and phantom composition are estimated to be 1%, which does not begin to account for the large discrepancy that is seen.

Presently, a median filter is applied to the images and this reduces the high frequency noise that is seen in the images. The question which now arises is where does this noise come from. Therefore, this is a possible area for more research to determine the origin of the noise and quantify it.

The change in sensitivity of the dosimeter to a change in field strength of the clinical scanner was investigated. The relaxivity for ferric ions at 3 Tesla was found to be 44% higher than that at 1.5 Tesla, whereas the relaxivity of ferrous ions showed no significant difference. This increase in relaxivity of the ferric ion, which translates into an increase in the dosimeter's sensitivity, is due to the fact that the hyperfine interaction plays a role in the relaxation of protons which hydrate paramagnetic ions.

This was confirmed by the good agreement of the relaxivity of the ferric ion with theory at 128 MHz (3 T). This is a new result that has not previously been reported in the literature.

Experiments were also conducted to observe the dosimeter's capability to handle clinical irradiation set-ups. Two experiments were performed: a head and neck study and a two catheter brachytherapy irradiation. The results obtained from these experiments were consistent with what was expected on the basis of independent measurements made using other dosimeters as well as plans made using treatment planning software. Therefore it can be concluded that this dosimeter is capable of handling clinical set-ups.

This dosimeter can perform well in the clinical environment as a relative dosimeter if relatively high doses are delivered which will allow the dosimeter to fall within the guidelines of accuracy of 5% set by the ICRU [ICRU 24 1976]. Also the following guidelines should be followed to ensure the best results:

- A dosimeter composition of 4% (by weight) gelatin, 1 mM ferrous sulphate and 0.05 M sulphuric acid.
- The parameter $\Delta R2$ should be used to minimize errors due to the imaging unit.
- Post-irradiation images should be acquired within 1 hour after irradiation to reduce the effects of diffusion of the ions.
- If using electron beams, radiation should not be imparted onto the exposed surface of the gel.

References

Appleby A, Christman E A, and Leghrouz A "Imaging of spatial radiation dose distribution in agarose gels using magnetic resonance" *Med. Phys.* **14** (3) 382-384 (1987)

Appleby A, Leghrouz A, and Christman E A "Radiation chemical and magnetic resonance studies of aqueous gels containing ferrous ions" *Radiat. Phys. Chem.* **32** (2) 241-244 (1988)

Attix F H "Introduction to Radiological Physics and Radiation Dosimetry" New York, U.S.A. John Wiley and Sons (1986)

Audet C, Keller B M, Schreiner L J "NMR Relaxation in the Fricke-Gelatin Dosimeter" *Proceedings of the SMRM Annual Meeting (abstract)* (1993)

Audet C "NMR-Dose Response Studies of the Gels used for 3-D Radiation Dosimetry by Magnetic Resonance Imaging" *Ph.D. Thesis* McGill University, Montreal, Canada (1995)

Balcom B J, Lees T J, Sharp A R, Kulkarni N S, and Wagner G S "Diffusion in Fe(II/III) radiation dosimetry gels measured by magnetic resonance imaging" *Phys. Med. Biol.* **40** 1665-1676 (1995)

Bengtsson M, Torbjorn F, Rodal J, Skretting A, and Olsen D "Measurement of dynamic wedge angles and beam profiles by means of MRI ferrous sulphate gel dosimetry" *Phys. Med. Biol.* **41** 269-277 (1996)

Bloembergen N, Purcell E M, and Pound R V "Relaxation effects in nuclear magnetic resonance absorption" *Phys. Rev.* **73** 678 (1948)

Bloembergen N "Proton relaxation times in paramagnetic solutions" *J. Chem. Phys.* **27** (2) 572-573 (1957)

Carr H and Purcell E M "Effects of diffusion on free precession in nuclear magnetic resonance experiments" *Phys. Rev.* **94** 630-638 (1954)

Chan M F and Ayyangar K "Verfication of Water Equivalence of FeMRI gels using Monte Carlo Simulation" *35th Annual Meeting of the AAPM* Washington DC (1993)

Crawley A P and Henklemen R M "Errors in T2 estimation using multi-slice multi-echo imaging" *Mag. Res. Med.* **4** 34-37 (1987)

deGuzman A, Gore J C, Schultz R J "Dose-response curves for gels infused with Fricke dosimeter by NMR" *Med. Phys. (abstract)* **16**(3) 457 (1989)

Dixon R L and Ekstrand K E "The physics of proton NMR" *Med. Phys.* **9** 807 (1982)

Duzenli C "Spin-spin relaxation rate MRI dosimetry using ferrous sulphate gelatin materials" *Ph.D. Thesis* University of Alberta, Edmonton, Alberta, Canada (1995)

Duzenli C, Sloboda R, and Robinson D "A spin-spin relaxation rate investigation of the gelatin ferrous sulphate NMR dosimeter" *Med. Phys. Biol.* **39** 1577-1592 (1994)

Duzenli C and Robinson D "Correcting for RF inhomogeneities in multi-echo pulse sequence MRI dosimetry" *Med. Phys.* **22** (10) 1645-50 (1995)

Eisinger' J, Shulman R G, and Szymanski BM "Transition metal binding in DNA solutions" *J. Chem. Phys.* **36** 1721-9 (1962)

Fransson A, Ericsson A, and Sperber G O "MRI Measurements of the Dependence on T1 of the echo amplitudes using a multi spin-echo scheme" *Mag. Res. Imag.* **11** 1185-1192 (1993)

Fricke H and Hart E J in "Radiation Dosimetry II Instrumentation" ed. Attix and Roesch New York, U.S.A. Academic 167-240 (1966)

Fricke H and Morse S "The chemical action of roentgen rays on dilute ferrous sulphate solutions as a measure of dose" *Am. J. Roentgenol. Radium Therapy Nucl. Med.* **18** 430-432 (1927)

Fricke H and Peterson B W "The relation of chemical, colloidal, and biological effects of rontgen rays of different wavelengths to the ionization which they produce in air I. Action of rontgen rays on solutions of oxyhemoglobin in water" *Am. J. Roentgenol. Radium Therapy Nucl. Med.* **17** (6) 611-620 (1927)

Gambarini G, Arrigoni S, Cantone M C, Molho N, Facchielli L, and Sichirollo A E "Dose-response curve slope improvement and result reproducibility of ferrous-sulphate-doped gels analysed by NMR imaging" *Phys. Med. Biol.* **39** 703-717 (1994)

Gore J C, Kang Y S, and Schultz RJ "Measurement of radiation dose distributions by nuclear magnetic resonance (NMR) imaging" *Phys. Med. Biol.* **29** (10) 1189-1197 (1984)

Hahn E L "Spin echoes" *Phys. Rev.* **80** 580-594 (1950)

Hazle J D, Hefner L, Nyerick C E, Wilson L, and Boyer A L "Dose-response characteristics of a ferrous-sulphate-doped gelatin system for determining radiation absorbed dose distributions by magnetic resonance imaging (Fe MRI)" *Phys. Med. Biol.* **36** (8) 1117-1125 (1991)

Hiraoka T, Fukuda N, Ikehira H, Hoshino K, Nakazawa K, Tateno Y, and Kawashima K "Digital Imaging of Dose Distributions by Magnetic Resonance" *Nippon Acta Radiologica* **46** (3) 503-506 (1986)

Hiraoka T, Hoshino K, Kawashima K, Kato H, and Tateno Y "A new gel using super absorbant polymer for mapping spatial dose distributions of electron beams by MR imager" *Med. Dos.* **18** 73-79 (1993)

Hughes D G "Errors in T2 values measured with the Carr-Purcell-Meiboom-Gill Pulsed NMR sequence" *J. Mag. Res* **26** 481-489 (1977)

ICRU Report 24 "Determination of Absorbed Dose in a Patient Irradiated by Beams of X or Gamma Rays in Radiotherapy Procedures" Bethesda, Maryland, U.S.A ICRU (1976)

Johns H E and Cunningham J R "The Physics of Radiology" 4th Edition Springfield, Illinois. Charles C. Thomas (1983)

Keller B M "Characterization of the NMR-Based Fricke-Gelatin Radiation Dosimeter" *M.Sc. Thesis* McGill University, Canada (1994)

Khan F M "The Physics of Radiation Therapy" 2nd edition Maryland, U.S.A Williams and Wilkins (1994)

Knoll G F "Radiation Detection and Measurement" 2nd edition New York, U.S.A John Wiley and Sons (1989)

Koenig S H and Brown RD "Relaxation of solvent protons by paramagnetic ions and its dependence on magnetic field and chemical environment: implications for NMR imaging" *Mag. Res. Med.* **1** 478-495 (1984)

Kron T and Pope J M "Dose distribution measurements in superficial x-ray beams using NMR dosimetry" *Phys. Med. Biol.* **39** 1337-1349 (1994)

Kron T, Rajanayagam V, and Pope J M "Fast T_1 imaging for the evaluation of diffusion in NMR dosimetry gels" *Med. Phys.(abstract)* **21** (6) 901 (1994)

Luz Z and Shulman R G "Proton Magnetic Resonance Shifts in Aqueous Solutions of Paramagnetic Metal Ions" *J. Chem. Phys.* **43** (10) 3750-3756 (1965)

Majumdar S, Orphanoudakis S C, Gmitro A, O'Donnell M and Gore J C "Errors in the measurement of T2 using multiple-echo MRI techniques" *Mag. Res. Imaging.* **3** 397-417 (1986)

Marcus Y "Ionic Radii in Aqueous Solutions" *J. Solution Chem.* **12** (4) 271-275 (1983)

Maryanski M J, Gore J C, Kennan R P, and Schultz R J "NMR relaxation enhancement in gels polymerized and cross-linked by ionizing radiation: A new approach to 3 D dosimetry by MRI" *Mag. Res. Imag.* **11** 253-258 (1993)

Maryanski M J, Schultz R J, Ibbott G S, Gattenby J C, Xie J, Horton D, and Gore J C "Magnetic resonance imaging of radiation dose distributions using a polymer gel dosimeter" *Phys. Med. Biol.* **39** 1437-1455 (1994)

Maryanski M J, Ibbott G S, Eastman P, Schultz R J, and Gore J C " Raditation Therapy dosimetry using magnetic resonance imaging of polymer gels" *Med. Phys.* **23** (5) 699-705 (1996)

Maryanski M J and Gore J C "Flip angle variations in large volumes of dielectric and conductive media at high fields: Implications for quantitation of relaxation times from images" *Proceedings of the SMRM Annual Meeting* (1992)

Meiboom S and Gill D "Modified spin-echo method for measuring nuclear relaxation times" *Rev. Sci. Instrum.* **29** 688-691 (1958)

Morris P G "Nuclear Magnetic Resonance Imaging in Medicine and Biology" New York, U.S.A. Oxford University Press (1986)

Nag S "High Dose Rate Brachytherapy: A Textbook" New York, U.S.A. Futura Publishing Co. Inc (1994)

Olsen D R and Hellesnes J "Absorbed dose distribution measurements in brachytherapy using ferrous sulphate gel and magnetic resonance imaging" *British Journal of Radiology* **67** 1121-1126 (1994)

Olsson L E, Petersson S, Ahlgren L, and Mattsson S "Ferrous sulphate gels for determination of absorbed dose distributions using MRI technique: basic studies" *Phys. Med. Biol.* **34** (1) 43-52 (1989)

Olsson L E, Fransson A, Ericsson A, and Mattson A "MR imaging of absorbed dose distributions from radiotherapy using ferrous sulphate gels" *Phys. Med. Biol.* **35** (12) 1623-1631 (1990)

Olsson L E, Westin B A, Fransson A, and Nordell B "Diffusion of ferric ions in agarose dosimeter gels" *Phys. Med. Biol.* **37** (12) 2243-2252 (1992)

Parker W A, Schreiner L J, Evans M D, and Audet C " Imaging of HDR Brachytherapy dose distributions using MRI and Fricke-gelatin dosimetry" *Med. Phys.* **21** (8) 1364-1365 (1994)

Podgorsak M B and Schreiner L J "Nuclear magnetic relaxation characterization of irradiated Fricke solution" *Med. Phys.* **19** (1) 87-95 (1992)

Prasad P V, Nalgiolglu O, and Rabbani B "Measurement of three-dimensional radiation dose distributions using MRI" *Rad. Res.* **128** 1-13 (1991)

Press W H, Teukolsky S A, Vetterling W T, Flannery B P "Numerical Recipes in C - The Art of Scientific Computing" 2nd Edition, New York, U.S.A, Cambridge University Press (1995)

Schreiner L J, MacTavish J C, Pintar M M, and Rupprecht A "NMR spin grouping and correlation exchange analysis: application to low hydration NaDNA paracrystals" *Biophys. J.* **59** 221-234 (1991)

Schultz R J, deGuzman A F, Nguyen D B, and Gore J C "Dose-response curves for Fricke-infused agarose gels obtained by nuclear magnetic resonance" *Phys. Med. Biol.* **35** (12) 1611-1622 (1990)

Solomon I "Relaxation processess in a system of two spins" *Physical Review* **99** (2) 559-565 (1955)

Stanton R and Stinson D "An introduction to Radiation Oncology Physics" Madison, Wisconsin, U.S.A. Medical Physics Publishing (1992)

Swallow A J "Radiation Chemistry" London. Longman 136-166 (1973)

Tortora G J "Principles of Human Anatomy" 6th edition. New York, U.S.A. Harper Collins Publishers (1992)

Vymazal J, Bulte J W M, Brooks R A, Frank J A, and Di Chiro G "T2 Field Dependence of Paramagnetic Ions and Magnetite" *Proceedings of the SMRM Meeting* (1992)

Zur Y and Stokar S "A phase cycling technique for cancelling spurious echoes in NMR imaging" *J. Mag. Res.* **71** 212-228 (1987)

Appendix

This is a typical routine that is used in MATLAB to convert ΔR2 images to dose images. The file is saved as a *.m file, and in MATLAB to call the routine the extension is dropped. For example if your routine was called dose.m, in MATLAB you would type "dose" at the prompt.

```
----------dose.m----------
clear                                   %clears the buffer

load mv1520p1.txt                       %loads your ascii ΔR2 image (256x256)

A=mv1520p1;A1=-A;                       %assigning a name for your image and
                                        %converting the -ve to a +ve. The -ve is
                                        %what the routine provides

smoothA2=medfilt2(A1,[3 3],[256 256]);  %Performing a 3x3 median filter

A2=smoothA2(56:195,63:202);             %Isolating your phantom from within
                                        %the matrix

A3=A2.*A2;                              %Prepares data for dose conversion
A4=13.7879.*(A2)+1.803.*(A3);           %A4 will be your Dose image using a
                                        %standard dose conversion factor

----------End of File----------
```

If you are going to use this program, do not include the information after the percent sign as these are just an explanation of the routine. Comments can be included in your *.m files but have to be on a separate line.

The following is a illustration of how a 3x3 median filter works: